ScuDo
Scuola di Dottorato ~ Doctoral School
WHAT YOU ARE, TAKES YOU FAR

Doctoral Dissertation
Doctoral Program in Electronics Engineering (29^{th}cycle)

Laser Diode Beam Spatial Combining

By

Hao Yu
******

Supervisor(s):
Prof. Guido Perrone, Supervisor
Prof. Renato Orta, Co-Supervisor

Doctoral Examination Committee:
Prof.ssa Elena Botta, Referee, University of Torino
Dr. Pierluigi Debernardi, Referee, CNR IEIIT
Prof. Gianni Coppa, Politecnico di Torino
Prof. Alberto Vallan, Politecnico di Torino
Dr. Andrea Braglia, OPI Photonics

Politecnico di Torino
2017

Declaration

I hereby declare that, the contents and organization of this dissertation constitute my own original work and does not compromise in any way the rights of third parties, including those relating to the security of personal data.

Hao Yu
2017

* This dissertation is presented in partial fulfillment of the requirements for **Ph.D. degree** in the Graduate School of Politecnico di Torino (ScuDo).

I would like to dedicate this thesis to my loving parents

Acknowledgements

There are a number of people who sincerely deserve my thanks fro their effort in supporting of my doctoral thesis. Special thanks goes to prof. Guido Perrone, who gave the perfect balance of technical direction and freedom in the pursuit of my research interests. A number of fellow colleagues contributed to the quality of this thesis through a sharing of ideas, technical expertise, and occasionally just plain hard work: Giammarco Rossi, Andrea Braglia, Alessio Califano and Mihaela Zelencu. I would like to thank all members of OPI Photonics S.R.L. for the fantastic environment for learning, friendly atmosphere, and technical support, and Prima Electro S.p.A. for the use of their equipment and opportunity to be a part of their group throughout the three years at Polito.

Finally, I would like to thank the sponsorship of the China Scholarship Council (CSC) and the support of the European Commission through the projects “white’R” (grant agreement No. 609228) and “Borealis” (grant agreement No. 636992) and the Regione Piemonte through the project “Ecoweld”.

Abstract

The growing demand for high-power laser diode modules for laser-based material processing machines has stimulated the development of a number of architectures that, taking advantage of multiple beam combination techniques, have allowed the realization of multi-emitter devices with unprecedented performance. However, these designs typically rely on roughly approximated relations, which have reached their limit of applications. Therefore, to further scale the output power and increase the brightness, new and more accurate models are necessary.

From the market point-of-view, the deployment of high-power multi-emitter modules is limited by the cost per emitted watt, which is proportional to the number of required optical elements and package assembly time. Cost reduction, therefore, requires, again, accurate models to properly optimize the package layout, but also new assembly strategies and tools.

The thesis analyzes in detail these two aspects - accurate models and assembly strategies and tools - and presents for both innovative solutions to help to push the technology beyond the current state-of-the-art.

In particular, for what concerns the multi-emitter model, a new relation to predict the beam quality at the pigtail fiber input by taking into account the impact of lenses and the distance between two adjacent chips in spatial beam multiplexing has introduced. The model is based on the propagation and transformation of paraxial Gaussian beams and analyzes, not only the impact of the choices on the focal length of each collimating or focusing lens but also of the truncation caused by their finite aperture. Then, as the model requires the knowledge of the individual laser chip beam characteristics, specific benches for the measurement of the near and far field emissions have been developed. The proposed model has been validated in different working conditions and found to lead to an error lower than 6%.

As for the multi-emitter assembly, an industrial grade procedure has been devised and a completely new approach based on back-propagation artificial neural network to automatically determine the optimal positioning of each optical element has been developed. The neural network is trained using ray tracing of Gaussian beams, starting from the emission characteristics of the laser chips. The new tool has been tested in practical cases with the most critical of all the components, the positioning of the fast axis collimator, obtaining a reduction of the assembly time of more than 50% with respect to current automatic assembly machines.

Finally, the design model and the assembly procedure have been applied to the development of a prototype of a multi-emitter module that, by exploiting spatial, wavelength, and polarization multiplexing of a plurality of chips emitting about 10 W each, delivers over 300 W in a 105/0.15 fiber pigtail, figures that represent a remarkable improvement over the current state-of-the-art. This result has been very challenging because it required the combination of theoretical, experimental, and technological aspects, not limited to photonics, but including also measurement theory, precision mechanics and thermal management.

Contents

List of Figures

List of Tables

Chapter 1

Introduction

1.1 High Power Lasers

High power lasers are finding increasing use in many fields, the most relevant being material processing (e.g., cutting and welding [1], but also the new and rapidly growing sector of the additive manufacturing from metal powders [2]), and, albeit with lower power, medical treatments (e.g., surgery [3] and solid tumor ablation [4–6]).

Targeting in particular industrial applications of Continuous Wave (CW) lasers for their relevance in the European manufacturing scenario, until few years ago the market was dominated by kilowatt range CO_2 lasers. Despite its versatility and the still superior effectiveness for cutting of thicker materials (e.g., above 5 mm) or of materials that benefit from its long wavelength (about 10 µm), this source has seen a rapid deployment decline in favor mainly of Fiber Laser (FL)s due to its very low wall-plug-efficiency[1], which severely limits further upscaling of power to improve processing speed and makes operative costs very high [7]. For instance, a common industrial laser, to generate 4 kW of optical power, has an electrical power consumption of almost 35 kW, not to mention additional 30 kW to 40 kW for the cooling system. Moreover, CO_2 lasers require cumbersome mechanical alignments

[1] Wall-plug efficiency is a parameter that takes into account the overall power conversion losses, from the mains supply to the optical output. In principle, this value should include losses in the power supply and also the power required for the cooling system, which can be significant for high-power lasers; however, it is commonly calculated based on the electric power delivered to the laser system, not including additional consumptions, for instance for cooling.

and complex free space beam delivery systems, which make their maintenance quite expensive. Due to these drawbacks, the share of CO_2 lasers dropped by 5% in 2015 and by 11% in 2016, as shown in Tab. 1.1. In comparison, FLs have shown a remarkable increase over the same period, while the combined sales of solid state and other lasers remained more or less flat.

Table 1.1 Industrial laser revenues by laser type (M$).

	2014	2015	2016
CO_2	$694.5	$656.7	$587.3
Y-TO-Y		-5%	-11%
FIBER	$1,483.6	$1,713.7	$1,902.6
Y-TO-Y		16%	11%
SOLID-STATE	$463.9	$463.4	$461.0
Y-TO-Y		0%	-1%
OTHER	$331.6	$346.3	$367.8
Y-TO-Y		4%	6%
TOTAL	$2,973.6	$3,180.1	$3,318.7
Y-TO-Y		6.9%	4.4%

Source: Strategies Unlimited

Further expanding the analysis in Tab. 1.1 to include some more years, it becomes evident that the recent market of high power lasers has been revolutionized by the appearance of fiber lasers, which are characterized by a higher than 30% wall-plug efficiency. This means that, for example, a commercial 4 kW fiber laser has an electrical power consumption of about 11 kW, with "just" additional 12 kW to 15 kW for the cooling system. Moreover, the beam delivery is simplified being the light generated directly within a fiber and there is no moving parts, like pumps. These features, which lead to increased reliability and lower ownership costs, have been the key for the remarkable success of FLs [8]: indeed, as shown in Fig. 1.1, FLs have already taken 31% share of the total laser market in 2015 and are expect to approach 40% level by 2020.

Current standard for material processing industrial machines is to be equipped with 3 kW to 4 kW FLs, but some 10 kW single mode and 100 kW multimode machines have already been proposed [9]. As FLs are pumped by semiconductors

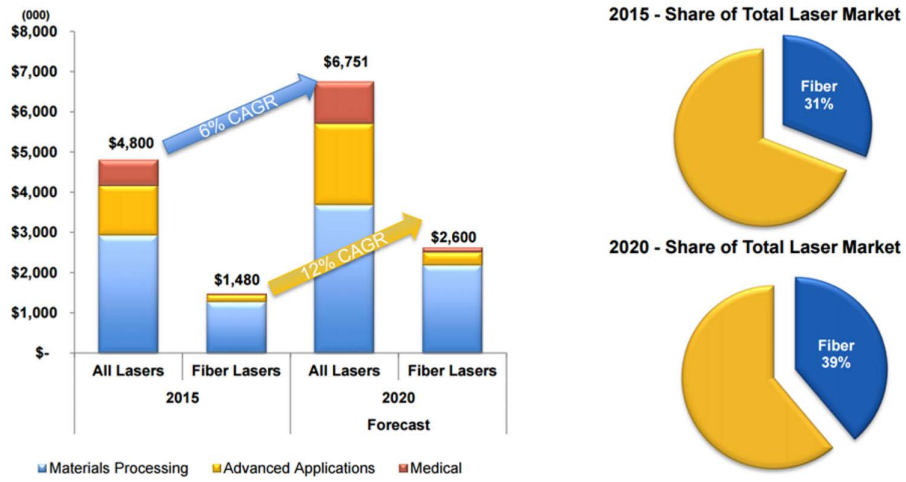

Fig. 1.1 High power laser market in different application sectors (source: Laser Focus World, Industrial Laser Solutions, Strategies Unlimited, Optech Consulting and IPG estimates).

LDs, their market share growth, furthermore combined with the continuous quest for higher power levels, has stimulated the development of new High Power semiconductor Laser Diode (HPLD) modules, capable of satisfying the requests in terms of pump power and brightness [2] with a reduced number of modules to simplify pump combing units. Besides for this main use, as the brightness improves, these HPLD modules are starting to find increasing applications as "direct diode" source in soldering, hardening and welding [10]. These new applications for HPLD are particularly attractive because of the higher energy efficiency, not having the pump-to-signal conversion loss of the active fiber.

The typical architecture of a high power fiber laser is shown in Fig. 1.2 [11]: it consists of a double cladding ytterbium-doped (or less commonly, thulium-doped) active fiber, in which the inner cladding is used to confine the pump, while the core to generate the laser signal. As a plurality of laser diode modules are required to reach the desired pump power level, a special device (usually a fused fiber combiner) is used to couple all these modules into the inner cladding of the active fiber. A couple of Fiber Bragg Grating (FBG)s then provides the feedback for the optical cavity. This basic system is often referred to as the Optical Engine (OE). Usually, the output power achievable from these OEs is up to about of 1 kW for about 1.6 kW of pump; therefore, to further scale the laser power, other devices, called "signal

[2] Brightness is the total power divided by the product of the mode area in the focus and the solid angle in the far-field. More details can be found in later sections.

combiners", are used to combine 3 to 7 OEs and reach the 3 kW to 4 kW output values commonly required by laser processing machines.

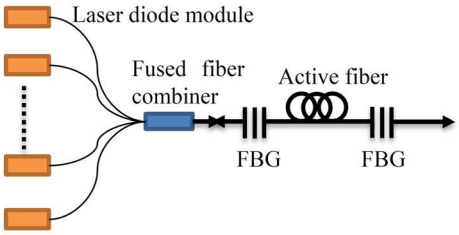

Fig. 1.2 Typical architecture of a fiber laser.

It is important to highlight that the pump source is not only one of the FL components that mostly affect its performance, but also its most expensive part. This provides another reason to justify the great effort made in research centers worldwide increase power and brightness while lowering the costs of HPLD modules.

1.2 Objective of the PhD Activity

The PhD research activity has been mainly aimed at studying new architectures for fiber-pigtailed high-power multi-emitter laser-diode modules to be used in the next generation of laser machines for material processing. In practice, this main objective translates into a series of intermediate goals, as listed in the following.

1. Survey of the literature to identify strong and weak points of available solutions and design of a compact and efficient layout able to overcome some of current limitations.
2. Development of the technology for the assembly of multi-emitters, from single chips[3] to the various optical components.
3. Set-up of benches for the characterization of chips and multi-emitter modules.
4. Experimental verification of some of the studied multi-emitter module configurations.

[3] In this work, when referring to chips, it is meant chips already mounted on proper carrier, what is also known as Chip on Carrier (CoC).

1.3 Background on Beam Combining

As mentioned in the previous paragraph, power scaling of HPLD modules with the highest possible beam quality[4] is of paramount importance for the realization of high performance and cost-effective fiber lasers. Today, state-of-the-art of HPLDs is to have wide area chips that emit about 10 W to 12 W. Further increase of power can be obtained with further broadening the chip active region transverse dimension, so as to lower the power density and improve the thermal dissipation; however, this worsens the beam quality and increases the cost. Therefore, aiming at modules able to deliver hundreds of watt, the only viable solution to scale power is through proper combination of single chips, either in the form of bars or of multi-emitters, the latter being currently the most popular because of the better brightness and the longer lifetime.

Laser chip beam combining can be coherent or incoherent. In theory, the number of chips that can be combined through coherent combination techniques is infinite, with the beam quality that remains that of the single beam, leading to very high brightness values. This approach, however, requires too strict control on the wavelength and the phase of each beam to be practically implemented in industrial grade products. In contrast, incoherent beam combining is the most popular because it is easy to realize and requires less stringent beam controls. Incoherent beam combining is implemented through three types of multiplexing, namely spatial (also known as beam stacking), wavelength and polarization multiplexing, usually applied in that order.

Considering incoherent beam combining, a multi-emitter module is basically a high precision mechanics metal box (typically copper alloy for the package and less expensive metals for the lid) that hosts some chips and related passive optical components (lenses, mirrors, polarizing beam splitter/combiner cubes, etc.) to shape the beams and couple them into an output delivery fiber, which is called the “pigtail”. An example of the external appearance of such devices is the commercial product in Fig. 1.3 [12]; a possibile internal architecture will be disclosed in later chapters. If properly designed, beam combining in multi-emitter modules allows also improving the overall brightness because more chips (hence more power) can be coupled into the same fiber pigtail. Indeed, while single chips exhibit divergence mismatch in

[4]Beam quality is measured through the BPP, a quantity that will be defined later in this chapter.

the two main orthogonal directions - the FA direction and the SA direction - so the overlap with fibers is not optimal, this overlap can be much better for the combined beams, leading to the brightness improvement. People in the field often express this by saying that " single chips do not fill well the fiber, while combined beams do". Just for reference, the divergence angle in the FA direction is in the 25° to 70° range (in terms of $1/e^2$ intensity), while in the SA direction is 5° to 10° (again, in terms of $1/e^2$ intensity) [13].

Fig. 1.3 Photo of a commercial 200 W fiber-coupled LD module.

In addition, when a module is based on LD bars instead of single emitters, to improve the beam quality of the SA, the beams must be rearranged and stacked [14, 15] as shown in Fig. 1.4 and in Fig. 1.5.

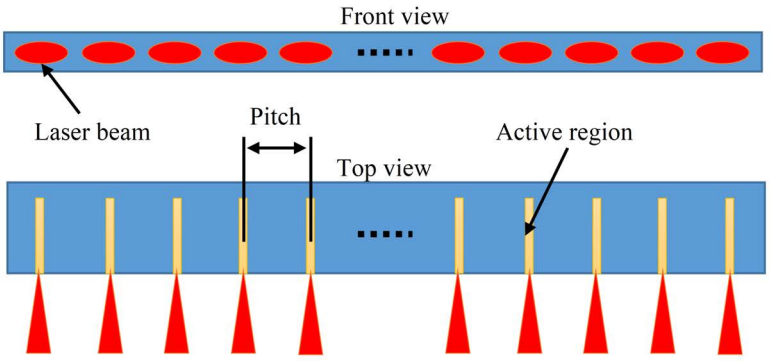

Fig. 1.4 Beams of LD bar.

Beam quality plays an important role, since it limits the maximal number of beams that can be coupled in a fiber of given core size and numerical aperture. In other words, the power of a multi-emitter module proportionally increases with the number of chips that can be coupled in the delivery fiber, and this number depends on the beam quality. The key parameter to evaluate the beam quality of laser beams is the BPP, which for Gaussian beams is defined as the product of the beam radius

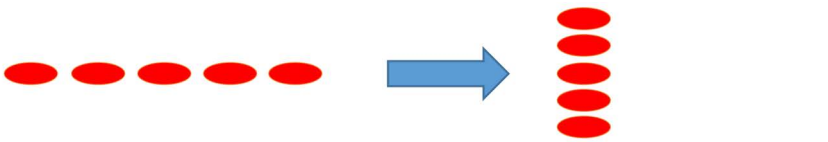

Fig. 1.5 Rearranging and combining of LD bar beams.

measured at the waist and the beam divergence half-angle measured in the FF. For non-Gaussian beams, second moments are used to define the beam radius and divergence. The smallest possible BPP is for diffraction-limited Gaussian beams, and, as it is evident from the definition, the higher the beam quality, the lower the BPP. The BPP is an optical invariant, so it cannot be improved by passive optical systems. Therefore, investigating the beam characteristics of LD stacks is helpful, not only to determine the power loss due to the mismatch with the BPP of the optical device to which the stack is coupled to (most often a fiber, so in the following a fiber will always be assumed as that optical device), but also to optimize the configuration of the LD stack itself.

However, despite its importance, literature and research so far have not clearly investigated the definition of the BPP for combined beams. Indeed, one of the most used relations is [16]:

$$\mathrm{BPP_{dia}} = (\mathrm{BPP_{slow}^2} + \mathrm{BPP_{fast}^2})^{1/2} \tag{1.1}$$

where $\mathrm{BPP_{dia}}$ is the combined diagonal BPP of the diode, and $\mathrm{BPP_{fast}}$ and $\mathrm{BPP_{slow}}$ denote the BPPs in the FA and SA directions, respectively. Another common relation found in previous literature is

$$\mathrm{BPP_{dia}} = \mathrm{BPP_{slow}} + \mathrm{BPP_{fast}} \tag{1.2}$$

The proof of these relations is reported only for Eq. 1.1 [17]; moreover, this equation does not take the impact of optical components and chip configuration into account. Furthermore, the maximal number of LD chips given by Eq. 1.1 is greatly underestimated. For instance, the diagonal BPP will be 5.14 mm mrad assuming $\mathrm{BPP_{fast}} = 7 \cdot 0.32 = 2.24\,\mathrm{mm\,mrad}$ and $\mathrm{BPP_{slow}} = 4.63\,\mathrm{mm\,mrad}$. However, the minimal diagonal BPP will be 6.87 mm mrad when the configuration is optimized,

which is 25% greater than the value given by Eq. 1.1. Underestimation of diagonal BPP tends to mislead designers and produce faulty designs.

Before presenting other results of the PhD activities, it is worthy recalling the fundamentals of beam combining techniques.

Beam combining identifies a group of technologies used to increase the output power and/or improve the brightness, with the minimal degradation of the beam quality, through the use of refractive, reflective and/or diffractive optical components. Combining techniques can be divided into two classes: coherent combining and incoherent combining [18], with the latter further subdivided into spatial overlapping (also known as "beam stacking"), polarization combining and wavelength multiplexing, as illustrated in Fig. 1.6.

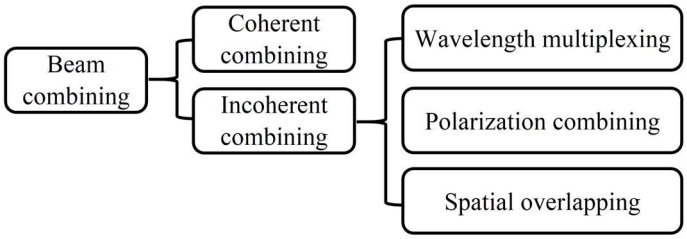

Fig. 1.6 Beam combining classification.

1.3.1 Coherent Combining

Coherent Beam Combining (CBC) controls the spectrum and the relative phase of each emitter to obtain constructive interference. Through CBC it is possible to obtain near-diffraction-limited outputs from large laser arrays; therefore, it is possible to combine a theoretical very large number of emitters while keeping the same beam quality of a single emitter. For example, Fig. 1.7 reports the scheme of an active CBC used to combine up to 218 semiconductor amplifiers, obtaining a total of 38.5 W CW output [19]. Despite its potential, however, this approach has never been used in commercial high power modules because it is very difficult and expensive to implement since it requires that the phases of the beams are controlled within a small fraction of wavelength.

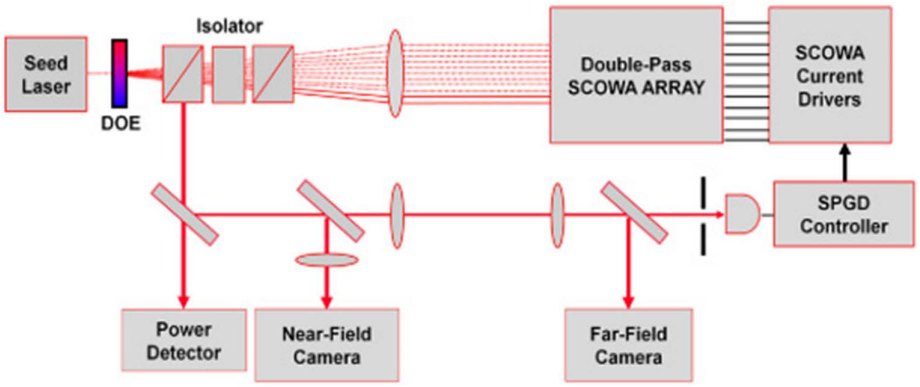

Fig. 1.7 Phase and spectrum control setup.

1.3.2 Incoherent Combining

Spatial Overlapping

Spatial overlapping, also called side-by-side beam combining or beam stacking, exploits the superposition of chips, operating at the same or different wavelengths, arranged in one direction (or, sometimes, in two directions). As mentioned in the Sec. 1.2, LD chips have a divergent beam in the FA and the SA directions, so the beams need to be collimated by using a sequence of a FAC and a SAC first, and then aligned. Fig. 1.8 shows an example of spatial overlapping of 7 emitters. Most multi-emitter modules overlap chips along the FA direction because the BPP in the FA direction is better than that in the SA direction. Considering a 8 W commercial high power diode chip as an example [20] (more details on the values of beam waists and divergences in the two directions can be found in Ch. 3), the FA BPP and the SA BPP are 0.32 mm mrad and 5.37 mm mrad, respectively, demonstrating that the SA beam quality is over 10 times worse than that of the FA.

One key parameter for evaluating the module performance is the radiance (or brightness). The diffraction-limited brightness is given by the power per unit area per unit solid angle [21]:

$$B = \frac{P}{(\pi R^2)\pi(0.61\lambda/R)^2} \tag{1.3}$$

where P is the power, R is the beam radius (defined for Gaussian beams at $1/e^2$) and λ is the wavelength.

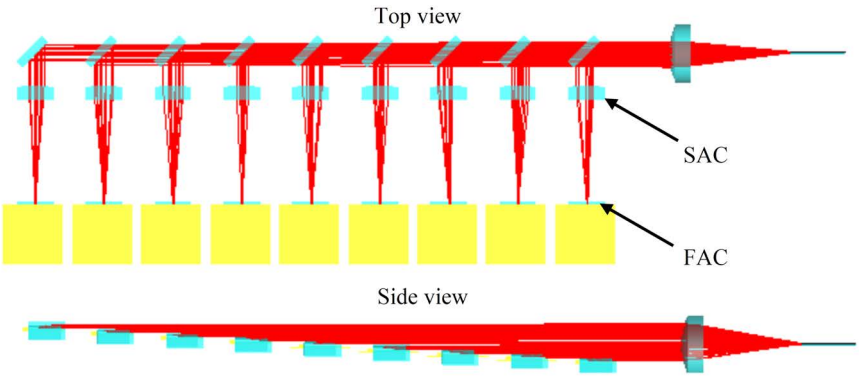

Fig. 1.8 Multi-emitter spatial overlapping.

Eq. 1.3 can be used also to calculate the brightness of non-diffraction-limited overlapped beams with simplifications. Assuming that each beam has the same power, beam size and divergence, the divergence of the stacked beams will not change but the power and the beam size tend to increase proportionally to the number of beams. Eq. 1.3 becomes:

$$B = \frac{NP}{NA\,\theta} \tag{1.4}$$

where N is the number of beams, A is the area of each beam and θ is the divergence of stacked beams. Therefore brightness cannot be improved using spatial combining; however, particular care should be used in selecting the optical components (FAC, SAC, and focusing lens) since they can cause a remarkable deterioration. More details will be discussed in Chapter 4.

Polarization Combining

Polarization combining is another popular technique used to scale power in high power modules, as the majority of semiconductor lasers naturally oscillate in a Transverse Electric (TE) mode [22]. Fig. 1.9 reports an example of a 18 emitters module that uses both spatial overlapping and polarization combining. Unlike spatial multiplexing, polarization combining increases the total output power while keeping the beam quality unchanged.

Although polarization combining ideally allows scaling the brightness by a factor of 2, it introduces also some critical aspects, besides for increasing the module cost. Indeed, at least one retarder (half-wave plate) and one polarizing beamsplitter cube are required to rotate the polarization of one of chip arrays and combine the two

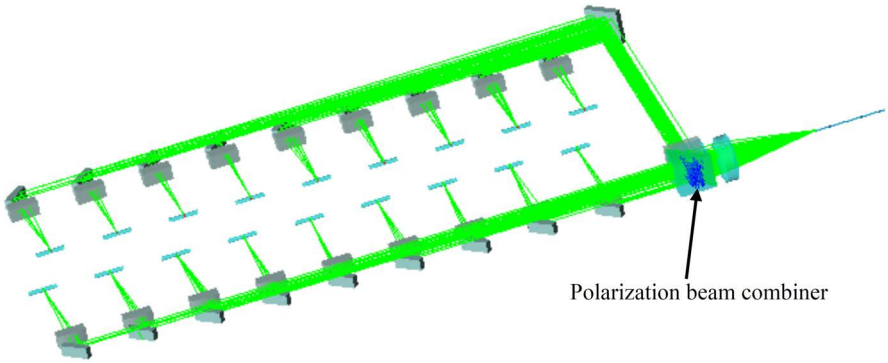

Fig. 1.9 Example of a module that uses both spatial and polarization combining.

orthogonally polarized beams, respectively. These two components represent an extra cost by themselves, but also impact on the module assembly procedure and duration, therefore adding also indirect costs. Furthermore, the non ideal behavior of the diode chips in terms of polarization purity and of the polarization beam combiner cause unwanted power leaking, which can induce deformations in the package as the local temperature increase, as shown in Fig. 1.10. Indeed, the polarization of wide strip multi-modes laser chips (the usual chips used in high power multi-emitter module) is mainly TE with a polarization ratio around 30:1 [13], which means that more than 3% of power will hit the wall of the package if there are no beam traps; this can cause deformations due to heat dissipation of the beams. In practice, more than 5% of power dissipation is always observed because the polarization ratio of wide strip chips is relatively low, and the transmittance and the reflectance of the polarized optical components are not 100%. Finally, residual beams could harm the chips themselves due to the reflections from the package walls. This risk can be reduced by proper design of the package layout that avoids the specular reflection backtracking to chips.

Wavelength Multiplexing

Wavelength multiplexing combines LD elements that operate at different wavelengths by using a dispersive optical component to overlap the beams from the emitters are shown in Fig. 1.11. Most common approaches make use of prisms, gratings or dichroic mirrors, each having its advantages and disadvantages. For instance, combining beams of different wavelengths through a prism or a grating can be done using a single optical component only, but poses strong requirements in terms

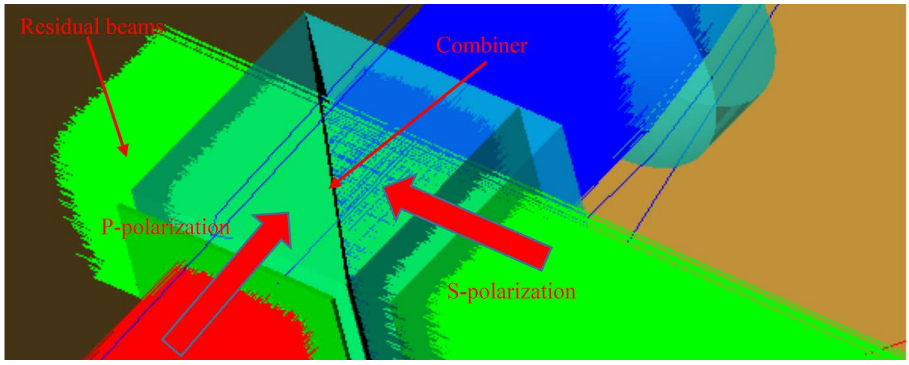

Fig. 1.10 Example highlighting a critical point in polarization combining due to the power leaking from the polarization combiner.

of wavelength stabilization and beam direction stability with driving current and temperature fluctuations. In contrast, using dichroic mirror allow relaxing these specifications, but requires $N-1$ components, being N the number of beams to be combined. Then, wavelength stabilization is not necessary if the central wavelength spacing among all the beams exceeds 25 nm.

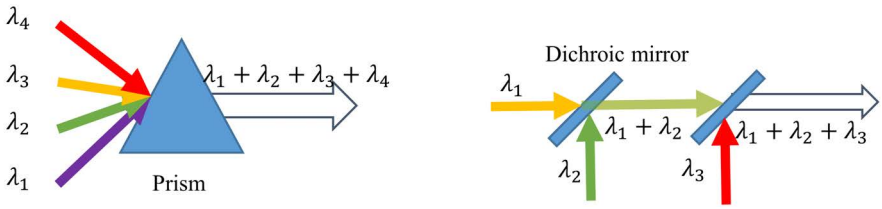

Fig. 1.11 Examples of wavelength multiplexing by using a prism (left) and a dichroic mirror (right).

The wavelength of each beams to be combined cannot be too close when the beams are emitted from non-locked broad area LD chips because the typical wavelength shift with temperature is around 0.3 nm/°C [23] and the central wavelength uncertainty of mirrors is typically ±10 nm [24, 25]. Fig. 1.12 [26] shows the example of multiplexing two different wavelengths, 905 nm and 940 nm. Both wavelengths shift from their nominal values and the spectral widths broaden as the current increases, but, since their spacing is more than 15 nm apart, a dichroic mirror whose 5% to 95% transition width is 6 nm can be safely used.

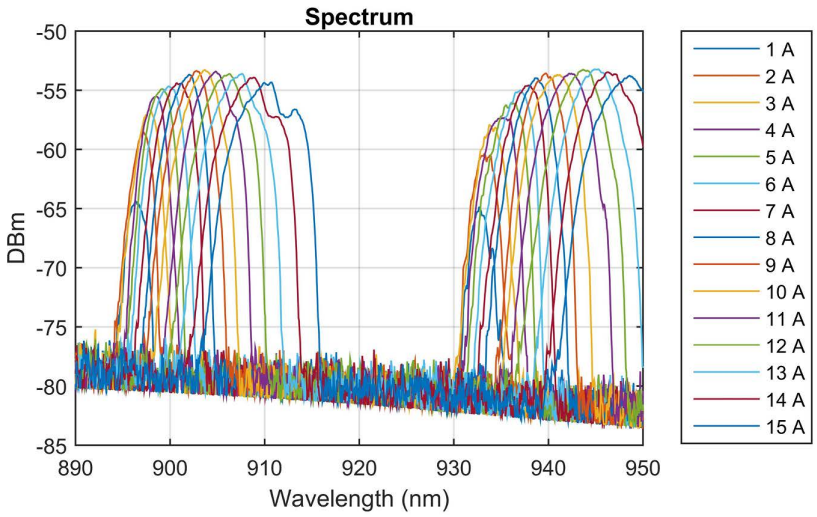

Fig. 1.12 Coarse combining of two wavelengths by using a dichroic mirror.

1.4 Main Contributions

The main achievement has been the design and experimental demonstration of different high-power modules that, by exploiting spatial, wavelength, and polarization multiplexing of a plurality of chips emitting about 10 W each, are able to deliver over 300 W in a 105/0.15 fiber pigtail, figures that represent a remarkable improvement over the current state-of-the-art. The activity has been very challenging because it required the combination of many theoretical, experimental, and technological aspects, not limited to photonics, but including also measurement theory, precision mechanics and thermal management.

In more detail, the most important outcomes from the PhD activities are listed in the following.

1. Derivation of an accurate formula to evaluate the BPP of multi-emitter modules, taking into account all the optical components included in the light path. The analysis of how the optical components used to collimate and focus the beams impact on the multi-emitter performance has been one of the key themes deeply analyzed during the PhD. First, it has been found that Eq. 1.2 can be actually used to set the minimum BPP of LD stacks, but the validity of this value is critically dependent on the configuration of beams and the choice of the optical components. Therefore, a new expression for the BPP of combined beams that takes into account the relation between the optical components and

the BPP has been derived [27]. This new relation has been experimentally validated and then applied to optimize some multi-emitter designs.

2. Investigation of a new algorithm to automatically assemble the most critical optical components, namely the fast axis collimator of diode laser chips, assisted by a BP-ANN; this approach resulted in a more that halving of the assembly time with respect to currently used automatic machines [28].

3. Identification of the bill-of-materials for the realizazion of prototypes of some multi-emitter configurations: choice of the optical components, definition of the chip-on-carrier attachment procedure and of the mounting strategy; analysis of the impact of components from different suppliers on the module optical and thermal performance.

4. Development of automatic setups for the NF and FF characterization of LD chips and modules and definition of operation procedures to ensure the consistency of the results.

Besides for these main activities, part of the time during the PhD has been also devoted to support the application of high power diode lasers in biomedical applications.

As not all of these activities can be fully described due to space and intellectual property limitations, the thesis will focus on the most innovative aspects only.

Chapter 2

Paraxial Gaussian Beam Propagation and Transformation

Paraxial Gaussian beam theory provides satisfactory approximations of the beam intensity radius, wavefront curvature radius and intensity radial distribution for reasonably well-collimated beams[29], but becomes inaccurate when beams diverge rapidly [30]. In more detail, for $w_0/\lambda \geqslant 0.9$, where w_0 is the $1/e^2$ intensity[1] radius of the beam waist, the paraxial approximation leads to accurate solutions, for $0.5 \leqslant w_0/\lambda \leqslant 0.9$ first-order corrections are necessary, for $0.25 \leqslant w_0/\lambda \leqslant 0.5$ higher order corrections must be used, and for $w_0/\lambda \leq 0.25$ the paraxial approximation totally fails even with the corrections. By substituting the definition of the BPP of near-diffraction-limited beam, $BPP = w_0\theta = \lambda/\pi$, into the ratio between w_0 and λ, it is possible to find out that the first-order corrections must be considered while using the paraxial model if the divergence is in the range of about 20° to 36°. As mentioned in Ch. 1, LDs are characterized by an elliptical beam that has near-diffraction-limited beam quality in the FA direction, but with a divergence that easily exceeds 25°. Nevertheless, if an error of about 10% can be accepted, the paraxial Gaussian model can be applied to study the propagation and transformation of the LD beams along the FA direction. As for the SA direction, the beam quality is much worser, but it has a much smaller divergence angle; in order to calculate the beam characteristics along this direction, M^2 factor[2] approximation is introduced.

[1] All the values in this chapter are defined at $1/e^2$ intensity unless otherwise specified.

[2] The M square factor, which is the ratio of the BPP of the beam to that of a Gaussian beam with the same wavelength, describes the deviation of the beam from a perfect Gaussian beam.

2.1 Fundamental Gaussian Beam Mode Propagation

One of the key parameters of a Gaussian beam is its Rayleigh range $z_c = \frac{\pi(w_0)^2}{\lambda}$, which is defined as the distance along the propagation direction of a beam from the waist to the place where the area of the cross section is doubled [31]. Using the definition of Rayleigh range, the beam intensity radius at a give distance $w(z)$, the wavefront curvature radius $R(z)$, and the intensity radial distribution in a cross section plane $I(r,z)$ of a Gaussian beam can be written as

$$w(z) = w_0 \left[1 + \left(\frac{z}{z_c}\right)^2\right]^{1/2} \tag{2.1}$$

$$R(z) = z + \frac{z_c^2}{z} \tag{2.2}$$

$$I(r,z) = I_0(z) \exp\left[-2r^2/w(z)^2\right] \tag{2.3}$$

where z is the axial distance along the propagation direction measured from the waist of the beam, r is the radial coordinate in a cross section plane at z, and $I_0(z)$ is the beam peak intensity in a cross section plane at z.

By applying Eq. 2.3 the power contained in different areas can be obtained easily. For example, the power portion of a circular Gaussian beam calculated at different intensity width is described by

$$\frac{\int_0^x 2I(r,z)\pi r dr}{\int_0^{+\infty} 2I(r,z)\pi r dr} \cdot 100\% = [1 - \exp(-2x^2/w(z)^2)] \cdot 100\% \tag{2.4}$$

where x is the beam radius corresponding to different intensity values. The intensity is reduced to half for $x = 0.59\omega(z)$, corresponding through Eq. 2.4 to 69.2% of the power, and to $1/e^2$ for $x = w(z)$, corresponding to 86.4%.

2.2 M^2 factor approximation

Eq. 2.1, Eq. 2.2 and Eq. 2.3 are valid for ideal diffraction-limited beams. Eq. 2.1 and Eq. 2.2 can be used also for non-diffraction-limited Gaussian beams by multiplying

the Rayleigh range by the M^2 factor. In practice it defines "how far" is the beam from an ideal Gaussian beam, which is known the have the best BPP possible. In formula, it is computed as the beam waist radius times the beam divergence divided by π/λ, the latter being the BPP of an ideal Gaussian beam. The M^2 factor cannot be introduced also in Eq. 2.3 because non-diffraction-limited Gaussian beams usually have top-flat intensity distribution. Of course, from its definition, it is clear that perfect Gaussian beams have $M^2 = 1$, while in general $M^2 \geqslant 1$.

The Rayleigh range of non-diffraction-limited Gaussian beam becomes

$$z_{\mathrm{c}} = \frac{\pi \omega_0^2}{M^2 \lambda} \tag{2.5}$$

The propagation of the beam can be roughly divided into two regions, Near Field (NF) and FF, depending on the distance from the source. NF region is defined for $z \ll z_{\mathrm{c}}$, whereas FF region for $z \gg z_c$. The beam radius is approximately equal to w_0 in NF and proportional to z in FF.

The transformation and propagation of a Gaussian beam in any optical system can be analyzed with Gaussian beam ray tracing method by tracing five rays only; more details will be given in the next section. When $z \to \infty$, the half divergence angle θ of a beam can be obtained by

$$\theta = \frac{w(z)}{z} = \frac{M^2 \lambda}{\pi w_0} = \frac{w_0}{z_{\mathrm{c}}} \tag{2.6}$$

If the axial thickness of a lens is small in comparison with the radii of curvature of its surfaces, it can be treated as a thin lens [32]. As only positive thin lenses are commonly used in LD beam measurement and multi-emitter module design, only positive thin lenses are considered here. With reference to the situation illustrated in Fig. 2.1, using the Cartesian sign convention, the relation between object and image position is

$$\frac{1}{p} + \frac{1}{q} = \frac{1}{f} \tag{2.7}$$

where p and q are, respectively, the object and image distances measured from the lens principal plane, f is the EFL of the positive thin lens, and h and h' are, respectively, the object and image heights. The magnification m produced by the

positive thin lens is then

$$m = \frac{h'}{h} = -\frac{q}{p} \tag{2.8}$$

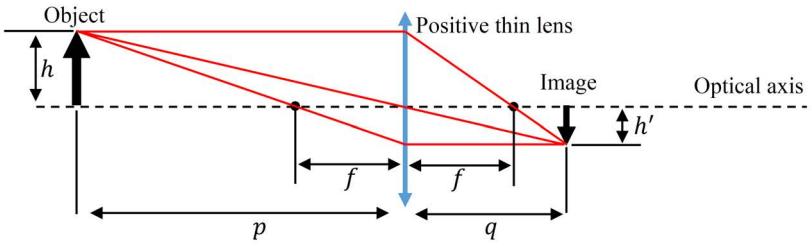

Fig. 2.1 Positive thin lens ray diagram.

Eq. 2.7 and Eq. 2.8 indicate that the magnification becomes infinite as $p \to \infty$, so, in other words, an infinitesimal focused spot can be achieved. However, this is not true because of diffraction, which limits the best focused spot from a perfect lens with a circular aperture to the Airy disk: considering a well-collimated beam at λ to be focused by a lens having EFL f and diameter D, it is possible to show that the diameter of the smallest spot is $2.44 f\lambda/D$.

For non-ideal Gaussian beams, Eq. 2.7 and Eq. 2.8, taking into account the M^2, become [33]

$$q = \frac{p\left(\frac{p}{f}-1\right) + f\left(\frac{z_c}{f}\right)^2}{\left(\frac{p}{f}-1\right)^2 + \left(\frac{z_c}{f}\right)^2} \tag{2.9}$$

In the meanwhile, the magnification m becomes

$$m = \frac{1}{\sqrt{\left(\frac{p}{f}-1\right)^2 + \left(\frac{z_c}{f}\right)^2}} \tag{2.10}$$

Fig. 2.2, Fig. 2.3, and Fig. 2.4 show the impact of M^2, respectively, on collimating, focusing and 1:1 imaging by applying Eq. 2.9. In particular, Fig. 2.2 shows the collimation of two beams by a 1 mm EFL lens. Both of beams are at the same wavelength of 920 nm and the same waist of 3 µm, but they have different beam quality, so one has $M^2 = 1$, whereas the other has $M^2 = 2$. Since the EFL of the lens is much larger than the Rayleigh ranges of two beams (for one is 0.12 mm and for

the other 0.06 mm), the beam radii at the lens are very different; after passing though the lens, both beams have the same divergence of 6 mrad, so the two beams overlap after having propagated for a certain distance.

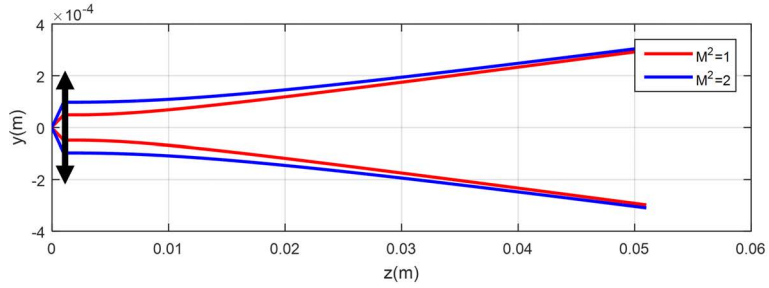

Fig. 2.2 Example of collimation of two beams having different quality.

An example of focusing two beams is illustrated in Fig. 2.3. The simulation is carried out under the same conditions used in the previous example except for the beam waist that changes to 60 µm. As seen in the figure, even if the two beams have the same beam waist radius, the spot size on the focal plane of the beam with $M^2 = 1$ is half of that of the other.

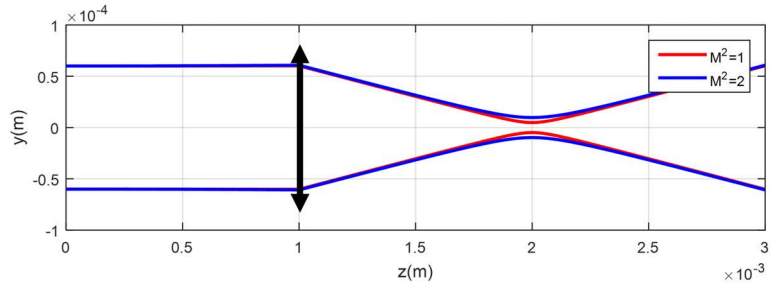

Fig. 2.3 Example of focusing of two beams having different quality.

As for 1:1 imaging, an example is shown in Fig. 2.4. Again, the main parameters are the same as in the collimation simulation, but the lens is moved from 1 mm to 2 mm so as to guarantee that the beam waist is located at twice the focal length. According to geometrical optics, the magnification in this case should be exactly equal to 1 and the image upside down; however, for the values of the example, even for $M^2 = 1$, Eq. 2.10 gives 0.992. This is because Eq. 2.10 becomes Eq. 2.8 only when $z_c \ll f$ (the lens is placed in the FF region), but when the EFL of the lens is in the order of z_c, the 1:1 imaging result is no longer valid.

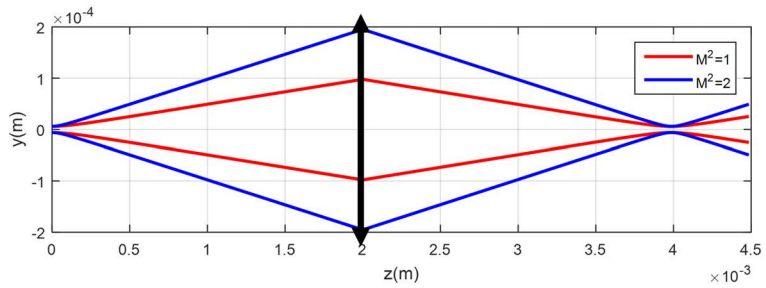

Fig. 2.4 Example of 1:1 imaging of two beams having different quality.

2.3 Ray tracing method

The propagation and transformation of a Gaussian beam by an optical system can be studied using an approach called Gaussian beam ray-equivalent model, which is derived from the well-known ABCD law of Gaussian beam transformation and whose terms consist solely of the heights and slopes of paraxial rays [34]. In practice, with this method tracing five ray trajectories (namely two waist rays, two divergence rays and one chief ray) is enough to calculate the intensity distribution at any point. An example of five ray trajectories of the Gaussian beam ray-equivalent model is shown in Fig. 2.5. Besides for requiring aberration free beams, the Gaussian beam ray-equivalent model imposes the further constrain of not having in the optical system components that tend to twist the beam.

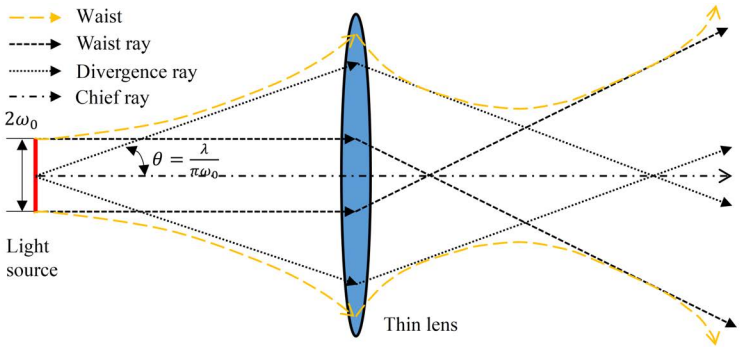

Fig. 2.5 Example of the five ray trajectories of the Gaussian beam ray-equivalent model for a lens.

Fig. 2.6 illustrates how to calculate the intensity at a given point P_0 using the Gaussian beam ray-equivalent model. The first step is to determine P_1, P_2 and P_3, which are the intersections of the waist ray, the divergence ray and the chief ray, respectively, with the plane normal to the chief ray and passing through P_0. Then,

an additional point, P_4, for which the intensity is $1/e^2$ of the intensity at P_3 must be identified; P_4 is on the same plane and its distance to P_3 is defined as

$$[(P_2P_3)^2 + (P_1P_3)^2]^{1/2}$$

Finally, the intensity at P_0 can be calculated as

$$I(P_0) = I_0 \exp\left(-2\left|\frac{P_0P_3}{P_4P_3}\right|^2\right) \tag{2.11}$$

where I_0 is the normalized input intensity.

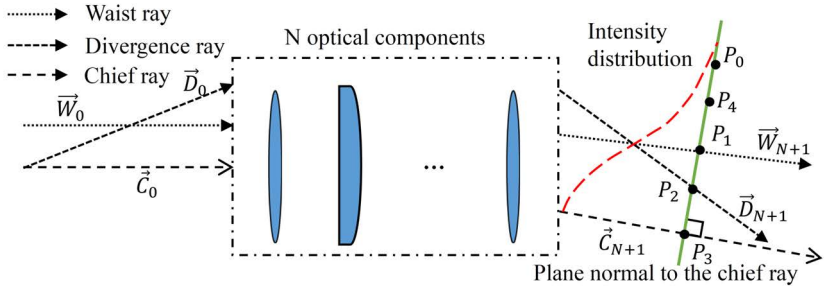

Fig. 2.6 Sketch identifying the points used to calculate the intensity at an arbitrary point using the Gaussian beam ray-equivalent model.

2.4 Large Divergence Angle Error Analysis

As mentioned at the beginning of this chapter, the range of applicability of the paraxial Gaussian beam propagation and transformation is given by the criterion $w_0/\lambda \leq 0.9$. By substituting $w_0/\lambda \leq 0.9$ into Eq. 2.6, the result $\theta \leq 0.35\,\text{rad}$ or $20°$ is obtained. Nevertheless, the paraxial approximation still returns acceptable values for beam divergence up to about $36°$, as it can be seen from the examples reported in Tab. 2.1 and Fig. 2.7. In Fig. 2.7, the solid lines are the results obtained from the NF to FF calculation by solving the Maxwell's equations, and the dotted lines with markers are computed directly by using the equation $\exp\left[-2(\theta/\theta_0)^2\right]$, where θ is the divergence angle and θ_0 is the $1/e^2$ divergence angle calculated by Eq. 2.6.

The beam propagation solving Maxwell's equations has been computed with a Finite-Difference Frequency-Domain (FDFD) method [35], using a freely available

Table 2.1 Comparison of half divergence angle as computed by solving Maxwell's equations and by applying the paraxial Gaussian beam theory.

Item	Ratio of w_0/λ	Maxwell's equations	Paraxial Gaussian beam theory
(a)	2	9.12	9.12
(b)	0.9	20.17	20.26
(c)	0.5	34.84	36.53
(d)	0.25	56.41	73.26

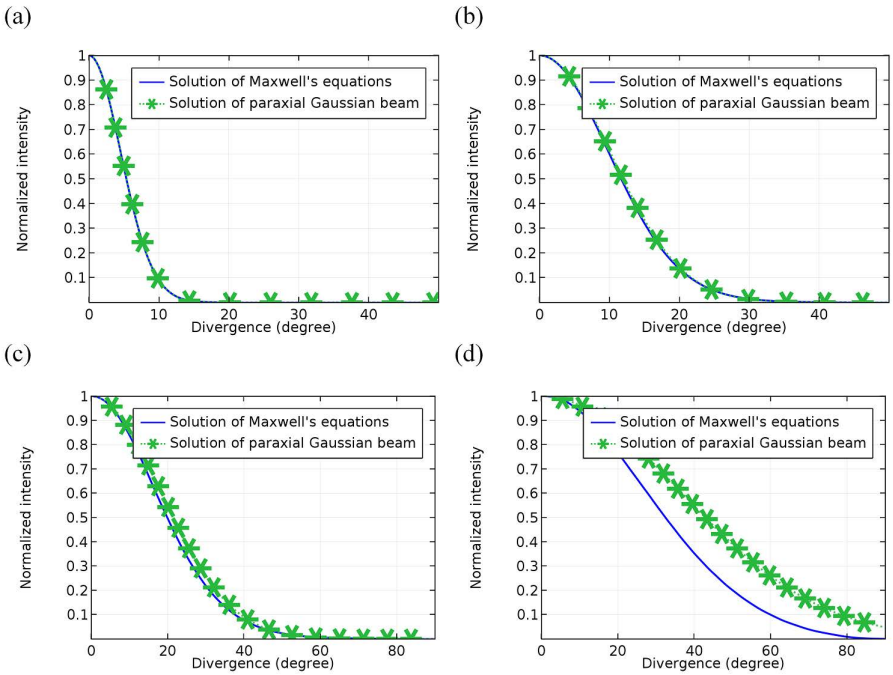

Fig. 2.7 Comparison between the FF from paraxial Gaussian beam theory and that from Maxwell's equations: (a) $w_0/\lambda = 2$, (b) $w_0/\lambda = 0.9$, (c) $w_0/\lambda = 0.5$ and (d) $w_0/\lambda = 0.25$.

software package [36] with the configuration shown in Fig. 2.8. The amplitude and the wavelength of the line source are set to $\exp(-y^2/w_0^2)$ and 920 nm, respectively.

After having computed the electric and magnetic field distributions on the surface enclosing the line source, the FF can be calculated from the NF using the Stratton-Chu formula [37] in 2D

$$\overrightarrow{E_{\mathrm{p}}} = \sqrt{\lambda}\frac{jk}{4\pi}\vec{r}_0 \times \int [\vec{n}\times\vec{E} - \eta_0\vec{r}_0 \times (\vec{n}\times\vec{H})]\exp(jk\vec{r}\vec{r}_0)d\vec{S} \tag{2.12}$$

where $\vec{E}$ and $\vec{H}$ are the electric and magnetic fields on the surface $\vec{S}$, $\vec{r}_0$ is the unit vector pointing from the origin $(0,0)$ to the field point p at the infinity but with a

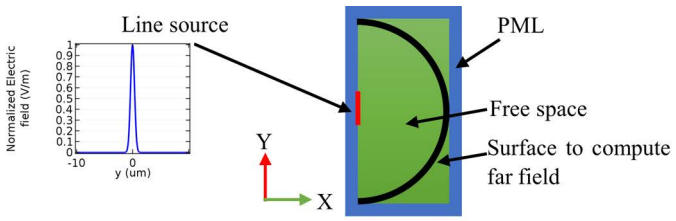

Fig. 2.8 Configuration used to compute the FF distribution with a FDFD simulator.

well-defined angular position (θ), $\vec{n}$ is the unit normal to the surface $\vec{S}$, η_0 is the impedance of the free space, k is the wave number, $\vec{r}$ is the radius vector of the surface $\vec{S}$ and $\vec{E}_{\mathrm{p}}$ is the calculated electric field in the direction from the origin towards point p.

Since the electromagnetic fields propagate in the free space, the FF radiation pattern is given by

$$I(p) = Re(\vec{E}_{\mathrm{p}} \times \vec{H}_{\mathrm{p}}{}^{*}) = \frac{1}{\eta_0}|\vec{E}_{\mathrm{p}}|^2 \tag{2.13}$$

Chapter 3

Laser Diode Beam Measurement

The design of efficient beam combining approaches requires the accurate characterization of the laser chip emission. This usually consists of five measurements, namely wavelength centroid and spectral width, power, NF, FF and astigmatism. As for wavelength and power, they are easy to measure with commercial specific instruments, such as optical spectrum analyzers (or wavelength meters) and power meters, respectively. On the contrary, NF, FF and astigmatism measurements imply the realization of ad-hoc setups and therefore these are the only measurements that are presented in this chapter.

A generic bench able to perform all three types of measurements has been designed and implemented. The result is shown in Fig. 3.1 and includes three movement stages (one 6-axis, one 5-axis, and one 3-axis), one Near Infrared (NIR) industrial CCD camera, and a custom-made jig to hold the laser chips while ensuring proper thermal dissipation through a water-cooled system. The 6-axis and 5-axis stages are driven by piezoelectric actuators and have a translation resolution of few hundredths of nanometer and a rotation resolution around 1 mrad; such high resolution performance is necessary to guarantee the accuracy and reliability of the measurements. The 3-axis linear translation stage has a resolution of 1 μm and it is used to move the CCD camera to measure the BPP and the divergence after collimation.

All bench components are automatically controlled by a software organized as in Fig. 3.2.

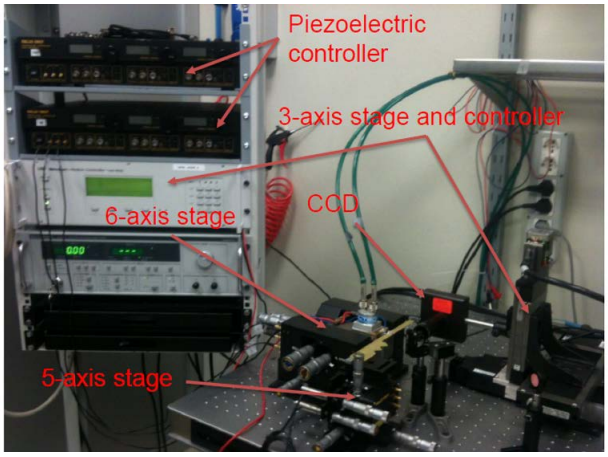

Fig. 3.1 Picture of the bench setup for the characterisation of laser chips and in particular for measuring their NF and FF distributions.

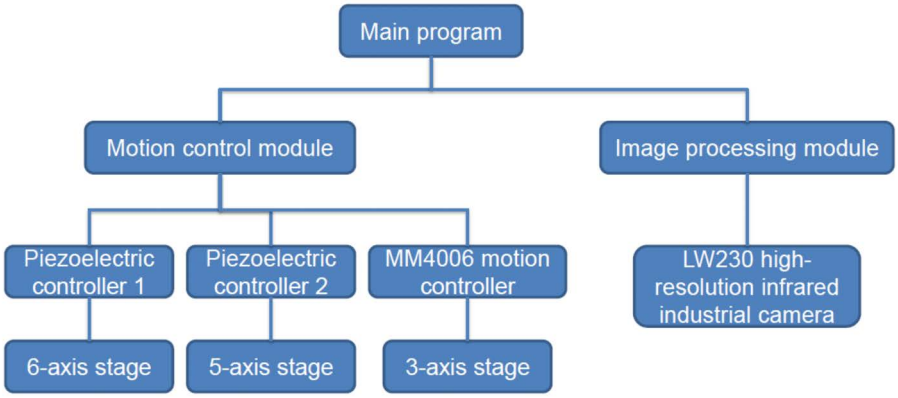

Fig. 3.2 Measurement bench control software diagram.

3.1 NF

The experimental setup to measure the NF of a LD is schematically shown in Fig. 3.3. The beam is collimated by the F1 lens, sampled using a wedge prism, further attenuated by a set of Neutral Density (ND) filters, focused by the F2 lens, and imaged onto a CCD camera. The two attenuation stages are necessary because, the NF distribution has to be measured also at full chip power; dealing with HPLDs, this means up to 10 W to 15 W, values that cannot be tolerated by the CCD camera. The F1 lens must be placed at a distance from the LD chip equal to its Front Focal Length (FFL). If we unfold the light path, then the distance between the F1 lens and the F2 lens will be the sum of the Back Focal Length (BFL) of F1 and the FFL of F2.

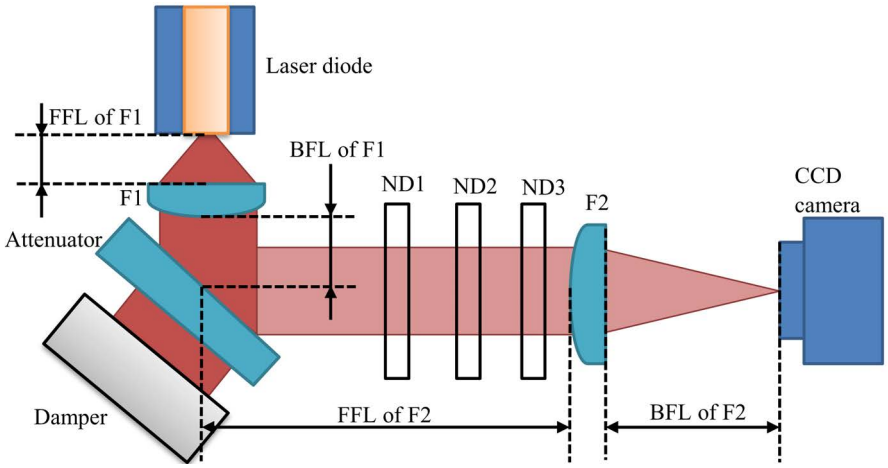

Fig. 3.3 Schematic representation of the NF measurement setup.

Consider the profile along the FA as a measurement example. Indicating with ${M_{\mathrm{FA}}}^2$ the beam quality factor, with $w_{0\mathrm{FA}}$ the beam waist, with f_1 the EFL of F1 and with f_2 the EFL of F2, the final beam waist locates exactly at the back focal plane of F2 and the new beam waist can be calculated by Eq. 2.10:

$$w_0'' = m_1 m_2 w_0 = \frac{f_1}{z_c}\frac{f_2}{z_c\prime} w_0 = w_0 \frac{f_2}{f_1} \tag{3.1}$$

Eq. 3.1 indicates that the beam quality and the choice of two lenses do not impact on the magnification, provided that all elements are placed at the theoretical positions. The accuracy of the magnification as determined from Eq. 2.10 has been discussed in Ch. 2 and found being acceptable even if the half divergence is up to 36°. However, a very large divergence affects the measurement if the Numerical Aperture (NA) of the lenses, especially of the F1 lens, is not compatible with the divergence angle. If this happens, part of the beam is truncated and diffraction effects should be taken into account; this will be further discussed in the error analysis section.

When the image is obtained from the CCD camera, the size of the active region beam waist w_0 along one of the two axes can be calculated considering that $w_0 = \frac{f_1}{f_2} d_{\mathrm{mea}}$, where d_{mea} is the size measured on the image. Take Fig. 3.4 as an example. The image area is 0.0528 mm × 3.0096 mm, and with $f_1 = 3.1$ mm and $f_2 = 100.1$ mm, the FA beam waist radius is 0.8 µm and the SA beam waist radius is 46.7 µm.

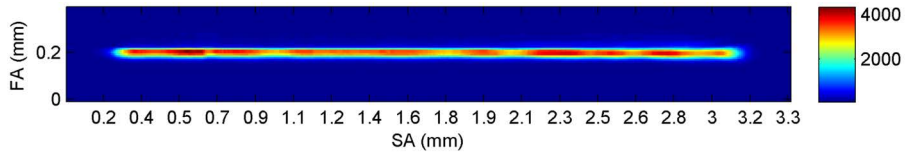

Fig. 3.4 Example of NF image on the CCD plane.

During the PhD activity several chips from different suppliers have been measured; examples are reported in Tab. 3.1 and Fig. 3.5. For all these measurements the temperature has been fixed at 25 °C through the cooling system.

Table 3.1 NF characteristic parameters (full width measured @ $1/e^2$ intensity) of some laser chips from different suppliers.

Parameter	Chip A	Chip B	Chip C	Chip D	Chip E	Chip F
FA width (μm)	1.91	1.61	1.92	1.60	1.61	1.62
SA width (μm)	131.20	117.09	105.82	95.58	93.46	99.80

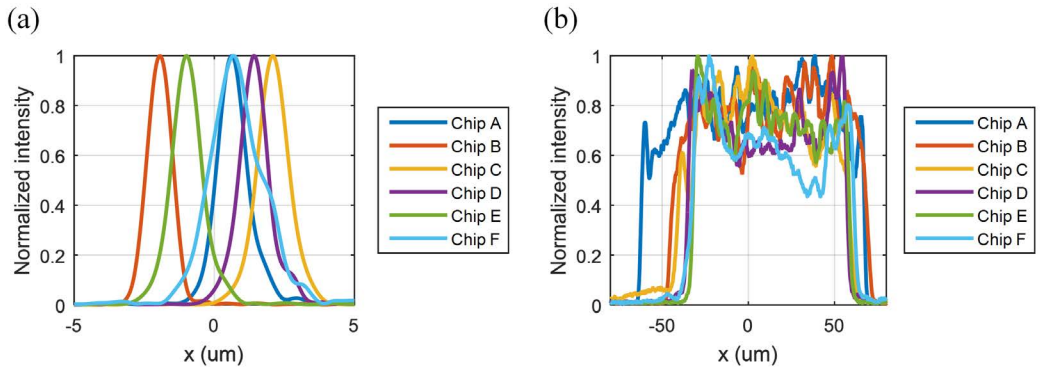

Fig. 3.5 NF intensity distribution of six chips from different suppliers: FA on the left and SA on the right.

3.2 FF

The FF is measured using the setup illustrated in Fig. 3.6. The setup is almost the same as that used to measure the NF, except for replacing the F1 lens with a larger EFL lens and inserting the F3 lens between the F2 lens and the CCD camera.

The conversion from the image size to the divergence is not apparent. If there is no F3 lens, the final beam waist radius is $w_0 \frac{f_2}{f_1}$ and the waist position locates at

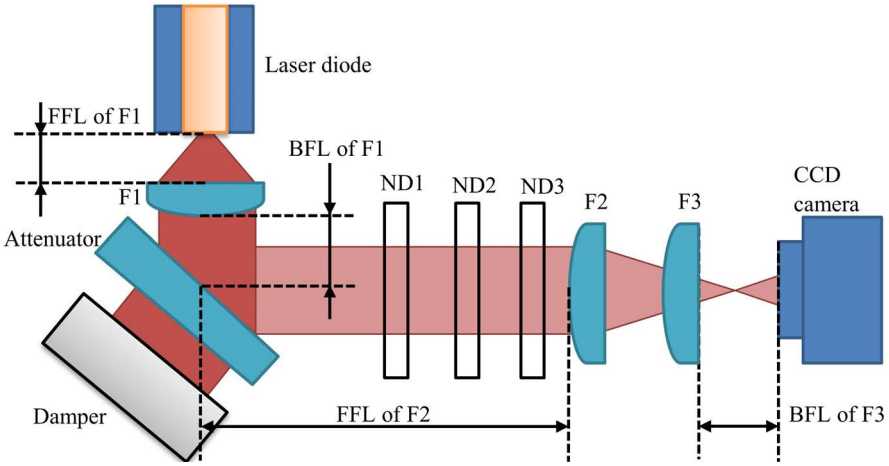

Fig. 3.6 Schematic representation of the FF measurement setup.

$2(f_1+f_2)$. With the F3 lens the new waist position will be

$$\begin{aligned} q &= \frac{-f_3\left(\frac{-f_3}{f_3}-1\right)+f_3\left(\frac{z_c}{f_3}\right)^2}{\left(\frac{-f_3}{f_3}-1\right)^2+\left(\frac{z_c}{f_3}\right)^2} \\ &= \frac{2f_3+f_3\left(\frac{z_c}{f_3}\right)^2}{4+\left(\frac{z_c}{f_3}\right)^2} \end{aligned} \tag{3.2}$$

where

$$z_c = \frac{\pi(w_0 f_2/f_3)^2}{M^2\lambda}$$

The new beam waist radius can be obtained by substituting Eq. 3.2 into Eq. 2.1:

$$w_0\frac{f_2}{f_1}\sqrt{1+\left(\frac{q}{z_c}\right)^2}$$

Since $w_0 f_2/f_1 \ll \lambda f_3$, the waist position and the waist radius can be simplified to $f_3/2$ and $w_0 f_2/2f_1$, respectively. Therefore the beam radius on the focal plane can

be written as:

$$w(f_3) = \frac{w_0}{2}\frac{f_2}{f_1}\left\{1+\left[\frac{M^2\lambda f_3}{\pi}\left(\frac{2f_1}{w_0 f_2}\right)^2\right]^2\right\}^{1/2} \approx \frac{M^2\lambda}{\pi w_0}\frac{2f_1 f_3}{f_2} \tag{3.3}$$

According to Eq. 2.6, which gives the definition of the half divergence angle θ of the beam, Eq. 3.3 can be rewritten as:

$$\theta = \frac{w(f_3)}{2}\frac{f_2}{f_1 f_3} \tag{3.4}$$

After having acquired the intensity distribution, the divergences θ along the two axes can be calculated as:

$$\theta = \frac{f_2}{f_1 f_3}\frac{d_{\text{mea}}}{2} \tag{3.5}$$

An example of the FF pattern for one of laser chips used in this work is shown in Fig. 3.7. From this image and with the help of Eq. 3.5, with $f_1 = 8\,\text{mm}$, $f_2 = 100.1\,\text{mm}$ and $f_3 = 49.8\,\text{mm}$, it is easy to determine the FA and SA full divergences, respectively 45.6° and 11.2°.

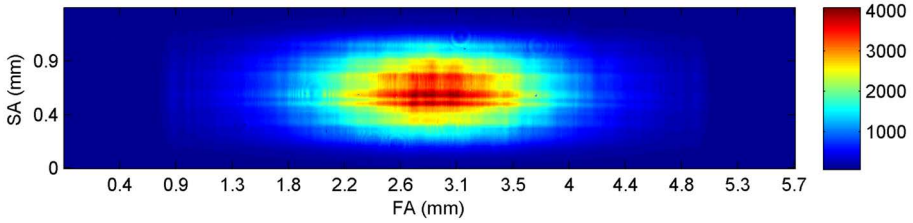

Fig. 3.7 Example of the FF image on the CCD plane of one of the considered high power laser chips.

FF measurements for chips from different suppliers have been carried out during the PhD activity. An example is shown in Tab. 3.2 and Fig. 3.8. It is worth mentioning that the beam is truncated in the all FA measurements so that a discontinuity occurs at around one tenth of the peak intensity.

Table 3.2 FF characteristic parameters of the same laser chips in Tab. 3.1.

Parameter	Chip A	Chip B	Chip C	Chip D	Chip E	Chip F
FA full divergence (°)	54.78	47.38	40.16	54.15	44.32	53.52
SA full divergence (°)	11.46	10.37	7.13	9.47	10.38	8.39

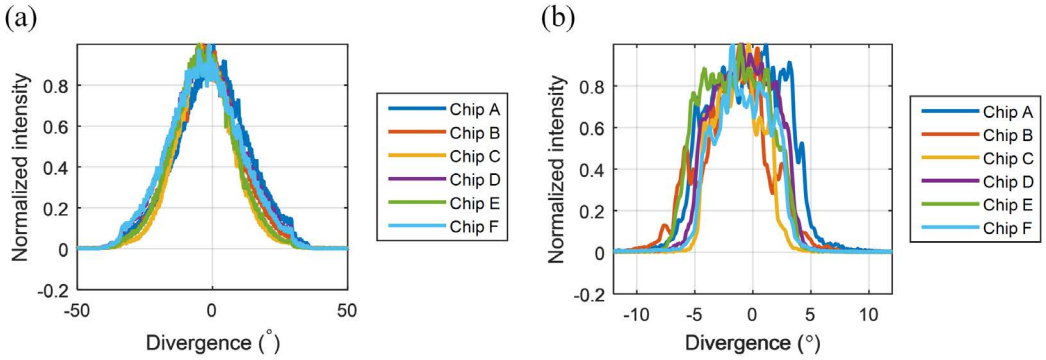

Fig. 3.8 FF intensity distribution for the six chips whose NF is reported in Fig. 3.5; FA is on the left and SA on the right.

3.3 Error Analysis

Both the paraxial Gaussian beam approximation and the non ideal behavior of the optical components contribute to the inaccuracy and the uncertainty of NF and FF measurements. Generally speaking, the components weight more.

3.3.1 Scalar Diffraction Theory

Solving Maxwell's equations by using FDFD method provides accurate solutions but consumes large amount of computational resource because the grid size must be in the order of wavelength, or even less. The smallest lens used in the experiment has the height of 450 µm and the light path is more than 100 mm, which requires 45 million grids. In order to less the time cost and the resource consumption, the scalar diffraction theory is chose to simulate the light propagation, transformation and truncation. The scalar diffraction theory is able to provide reliable solutions when the ratio w_0/λ is low, which can be learn from Fig. 3.9.

The errors introduced by the paraxial approximation and the beam truncation can be evaluated using the scalar diffraction theory. This approach allows computing the unknown complex field $U(\vec{x_0})$, where $\vec{x_0}$ is an observation point depending on

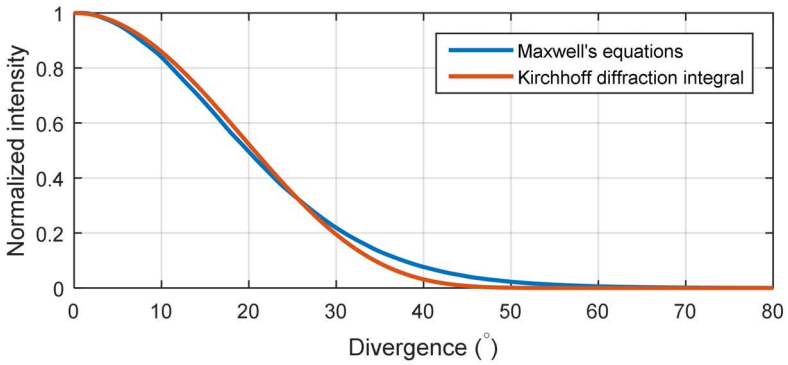

Fig. 3.9 Comparison between solving Maxwell's equations and Kirchhoff diffraction integral when $w_0/\lambda = 0.5$.

the spatial coordinates $\vec{x_0} = (x_0 y_0 z_0)$, from the complex field $U(\vec{x})$. Considering the Green's function

$$G(\vec{x}) = \frac{exp(jkr)}{r}$$

which represents a unit-amplitude spherical wave with $r = \|\vec{x_0} - \vec{x}\|$, the integral theorem of Kirchhoff can be expressed as [38]:

$$U(\vec{x_0}) = \frac{1}{4\pi} \int \int_S \left[U(\vec{x}) \frac{\partial G(\vec{x})}{\partial n} - G(\vec{x}) \frac{\partial U(\vec{x})}{\partial n} \right] \mathrm{d}s \tag{3.6}$$

where S indicates an arbitrary closed surface surrounding $\vec{x_0}$ and $\frac{\partial}{\partial n}$ denotes differential operator along the inward normal to S.

All lenses in the analysis are simplified as thin lenses, but with finite aperture. Fig. 3.10 illustrates the light propagation simulation of the NF measurement. Only the F1 lens suffers from the limited aperture problem, which therefore emphasised in the figure. In the simulation, the amplitude of the field outside the aperture is set to zero. The role of the lens is to change the phase of the incident field as [39]:

$$U'(x,y) = t(x,y)U(x,y) \tag{3.7}$$

where (x,y) denotes the position located on the plane perpendicular to z axis, $U'(x,y)$ is the complex field immediately behind the lens, $t(x,y)$ is the phase transformation function of lens and $U(x,y)$ is the incident complex field. The phase transformation function has the form:

$$t(x,y) = \exp\left[jk\phi(x,y)\right] \tag{3.8}$$

where $\phi(x,y)$ is the phase delay suffered by the wave at coordinates (x,y) in passing through the lens. Let the left surface radius of curvature of the lens, the right surface radius of curvature of the lens and the refractive index of the lens be R_1, R_2 and n, then the EFL of the lens f is defined by the so-called "lens-maker" equation:

$$\frac{1}{f} = (n-1)\left(\frac{1}{R_1} - \frac{1}{R_2}\right) \tag{3.9}$$

Since all lenses are assumed to be thin lens, the distance between the left surface and the right surface is negligible compared to R_1 and $R2$. And the phase delay becomes:

$$\phi(x,y) = jk\left[n\Delta_0 - (n-1)\frac{x^2+y^2}{2}\left(\frac{1}{R_1} - \frac{1}{R_2}\right)\right] \tag{3.10}$$

where Δ_0 is the constant phase factor introduced by the center thickness of the lens. Substituting Eq. 3.9 and Eq. 3.10 into Eq. 3.8, and neglecting the constant phase factor, the phase transformation function can be rewritten as:

$$t(x,y) = \exp\left[-j\frac{k}{2f}(x^2+y^2)\right] \tag{3.11}$$

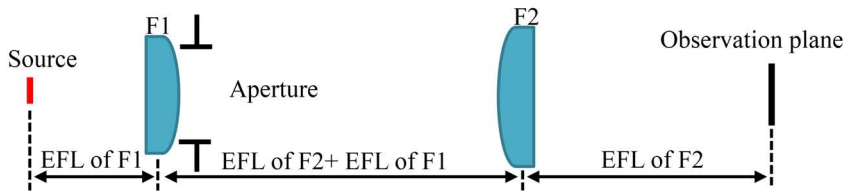

Fig. 3.10 Schematic of the configuration for the NF measurement setup as considered in the scalar diffraction simulation.

3.3.2 Paraxial Gaussian Beam Approximation

The error comes from two parts: the approximation in Eq. 3.3 and the model itself. It is easy to prove that the error brought by the former one is negligible. For instance, if $w_0 = 0.8\,\mu\text{m}$

$$\frac{M^2\lambda f_3}{\pi}\left(\frac{2f_1}{w_0 f_2}\right)^2 \approx 410$$

which is much greater than 1, hence the error is only $1/(410+1)\times 100\% = 0.2\%$. .

As for the error from the model, Fig. 3.11 indicates that the difference for $w_0/\lambda = 0.25$ case is few percent. However, it is notable that the measured value needs to be converted by taking the inverse tangent of the divergence in the FF measurement. Or two tails will exceed 90° like Fig. 3.12(a). In these two simulations, the aperture is infinite so as not to disturb the light propagation.

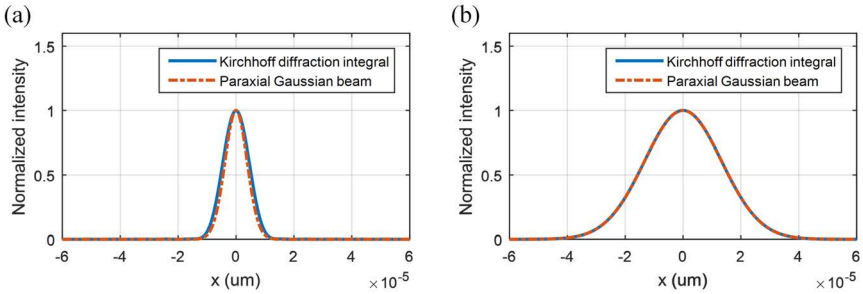

Fig. 3.11 NF measurement simulation results. (a) $w_0/\lambda = 0.25$ and (b) $w_0/\lambda = 0.87$.

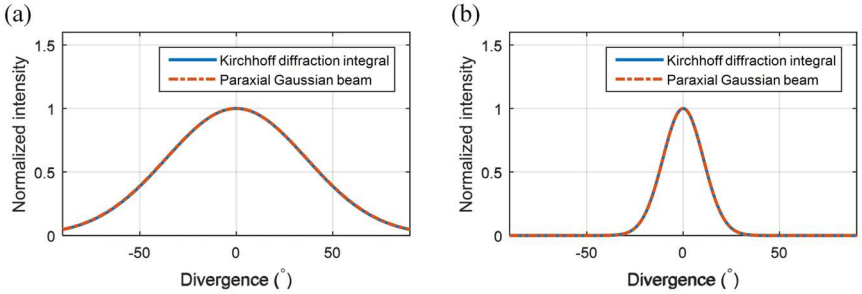

Fig. 3.12 FF measurement simulation results. (a) $w_0/\lambda = 0.25$ and (b) $w_0/\lambda = 0.87$.

3.3.3 Non Ideal Components

Since all the considered optical components are optimized for the specific application in which they are used, they introduce a negligible error due to no aberrations. Hence, the main impact comes from the limited NA of F1 lens during the FA measurement, as in the case depicted in Fig. 3.8(a), where the tails of the chip A's FA beam are cut and this worsens the beam quality due to diffraction. Fig. 3.13 and Fig. 3.14 show the simulation of the effect of a finite aperture. In the simulations the NA of all lenses is set to 0.5 and it is easy to prove that, with the beam characteristics of the chip considered in this research, only F1 lens introduce truncations, especially when the beam divergence is greater than 30°.

If the criteria $a/w(z)$ - where a is the aperture radius and $w(z)$ is the beam radius immediately behind the aperture - is used for defining the level of truncation, Fig. 3.13(a) and Fig. 3.14(a) can be called "strong truncation", and Fig. 3.13(b) and Fig. 3.14(b) "weak truncation" [33], respectively. It is equivalent to worsen the beam quality in $w_0/\lambda = 0.25$ case. Apart from the simulation, Fig. 3.15 refers to the measurement of a chip whose FA half divergence angle is much greater than the NA of F1 lens.

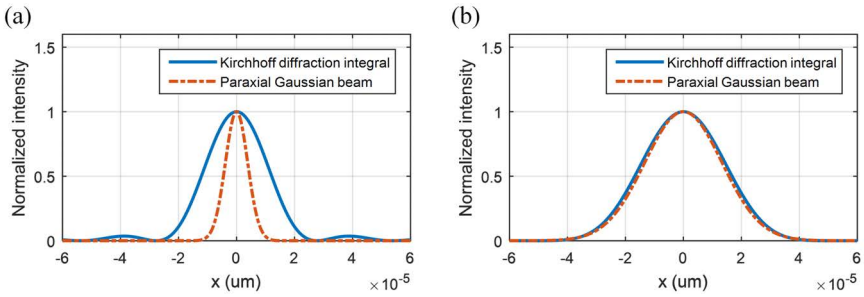

Fig. 3.13 Simulation results of NF measurement with finite aperture: (a) $w_0/\lambda = 0.25$ and (b) $w_0/\lambda = 0.87$.

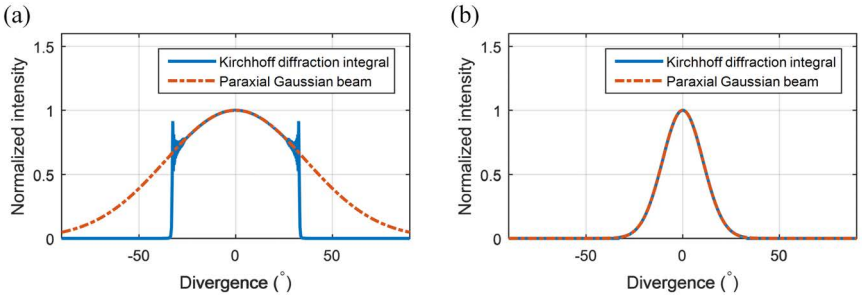

Fig. 3.14 Simulation results of FF measurement with finite aperture: (a) $w_0/\lambda = 0.25$ and (b) $w_0/\lambda = 0.87$.

The other device contributing to the uncertainty is the CCD camera. The camera used for both setups is the Lw230 [40], which has the pixel size of 4.4×4.4 µm. Considering the magnification of the optical system 30X, the uncertainty due to CCD pixel size will be around ±0.13 µm. An improvement can be obtained by replace the F1 lens with smaller EFL lens, for example 0.3 mm instead of 3 mm. The result of this lens change on the NF measurement is shown in Fig. 3.16: the uncertainty is reduced to ±0.01 µm. Taking for example Chip A, this measurement changes to 1.824 µm instead of 1.91 µm.

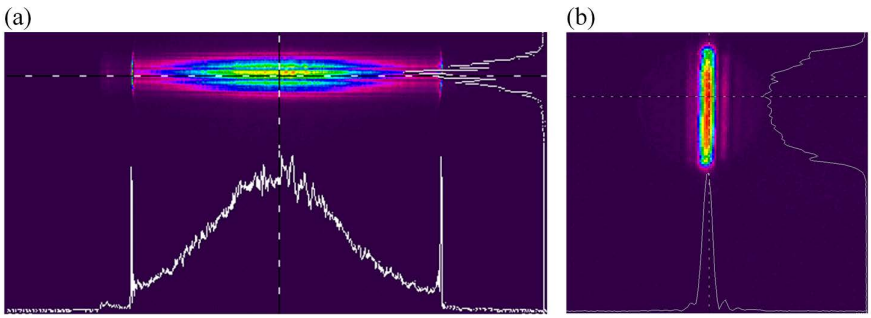

Fig. 3.15 NF and FF of large divergence laser beam: (a) FF, and (b) NF.

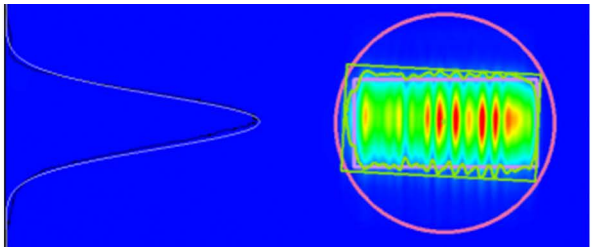

Fig. 3.16 NF measurement performed with a 300 um EFL FAC.

3.4 M^2 Factor

A possibility to evaluate the M^2 factor is to compute it from the beam waist (from the NF measurement) and the divergence (from the FF measurement) using its definition: $M^2 = w_0\theta\pi/\lambda$. Another approach is to directly measure it by scanning the beam along its propagation direction. Assuming that the beam waist radius, the wavelength and the position of beam waist are w_0, λ and z_0, respectively, squaring both sides of Eq. 2.1 gives:

$$w^2(z) = w_0^2\left\{1+\left[\frac{M^2\lambda(z-z_0)}{\pi w_0^2}\right]^2\right\} \tag{3.12}$$

where z is the axial distance along the beam propagation direction. Eq. 3.12 can be easily fit from measurements of the beam waist radius taken for different positions, so to estimate the M^2 factor. In practice, however, this is not so simple because of the divergence angle along the FA that makes impossible for the camera capture the beam after a few centimetres. Hence, the beam is usually collimated and then measured. Fig. 3.17 shows the example of beam scanning along the FA. In that case the beam was collimated by a 600 µm EFL FAC and captured along its propagation direction. Unfortunately, the FAC was not fixed perfectly, so the divergence increased

from the theoretical value of 1.33 mrad to more than 1.42 mrad. Anyway, scanning a collimated beam requires measuring huge amount of samples along the propagation direction because of relatively long Rayleigh range: in the 600 µm EFL example, Rayleigh range was 173 mm and this implies long measurement time and thus cost. This can be overcome by adding a focusing lens, as shown in Fig. 3.18, to make the beam diverge and thus shorten the measurement time.

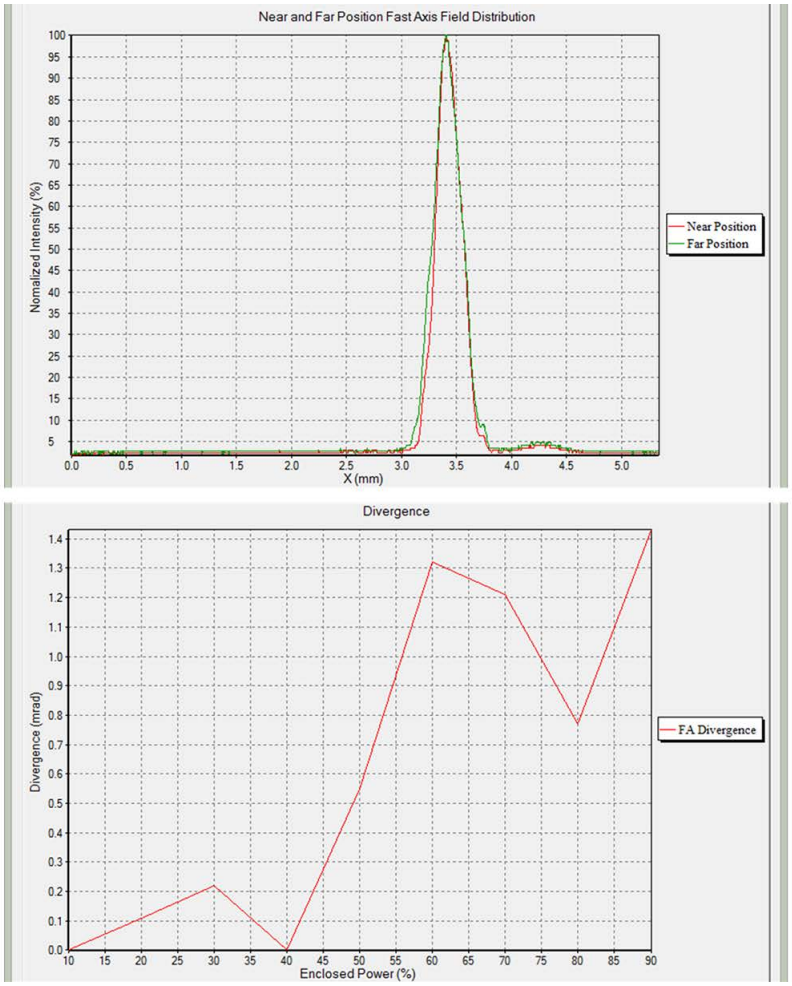

Fig. 3.17 Scanning of a collimated FA beam: top picture for the beam profile at different positions, and bottom picture for the power enclosed in different divergences.

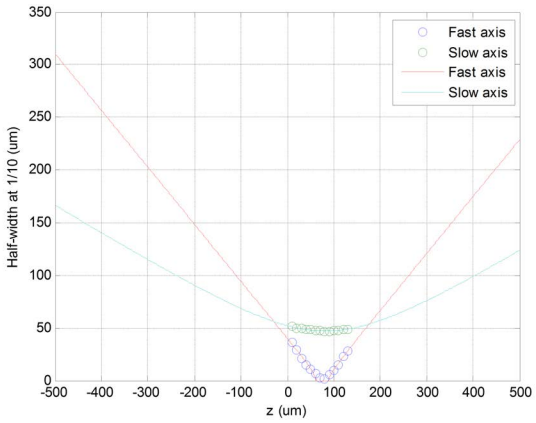

Fig. 3.18 Example of focusing of a well-collimated beam for shortening the Rayleigh range and thus the M^2 measurement time.

3.5 Astigmatism

HPLD chips emission is broader along the SA direction than in the FA direction and exhibits worse beam quality in the SA direction than in the FA direction. This is equivalent to a model where the light is emitted from two different points in the two planes, as illustrated in Fig. 3.19. Since the beam from LD is astigmatic, a single aspheric lens is not capable of collimating the FA and the SA together. Hence the moving LD method is used to measure the astigmatism [41]. First of all, preparing the setup as used in the NF measurement. Secondly, moving the LD toward to the F1 lens until the focused spot reaches its minimum along the FA direction and recording the chip position as z_1. Thirdly, keeping the movement of the chip until the focused spot is minimal along the SA direction and writing down the chip position as z_2. Finally, calculating the astigmatism, which is equal to $|z_2 - z_1|$. The astigmatism of the Chip A is 23 µm.

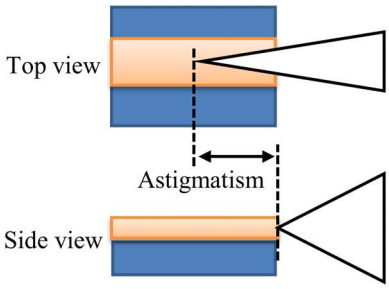

Fig. 3.19 Demonstration of the diode astigmatism.

Chapter 4

Spatial Overlapping

As mentioned in Ch. 1, the minimum BPP of spatially combined beams critically depends on the choice of the optical components used to collimate and focus them. In the following sections a new expression for calculating the minimal diagonal BPP of LD stack taking into account the contributions of such optical components will be described; then this expression will be used to evaluate the best combination of FAC, SAC, FA focusing lens and SA focusing lens, providing also some optimization examples. Part of the results reported in this chapter have been published in [27], [42], and in [43].

4.1 Theory

For sake of simplicity, but without losing generality, some assumptions can be made.

1. Although the beam emitted by the single LD chip has an elliptical shape, as depicted in Fig. 4.1-left, it can be approximated with a rectangle, as in Fig. 4.1-right, where $w_{0\mathrm{FA}}$, $w_{0\mathrm{SA}}$, θ_{FA}, and θ_{SA} are the beam waist[1] and the divergence of the FA and the SA, respectively.

2. The beam divergence after collimation is negligible.

3. All the beams emitted from the various LDs are incoherent with respect to each other and thus there is no interference.

[1] As already pointed out in previous chapters, all these widths are measured at $1/e^2$ intensity.

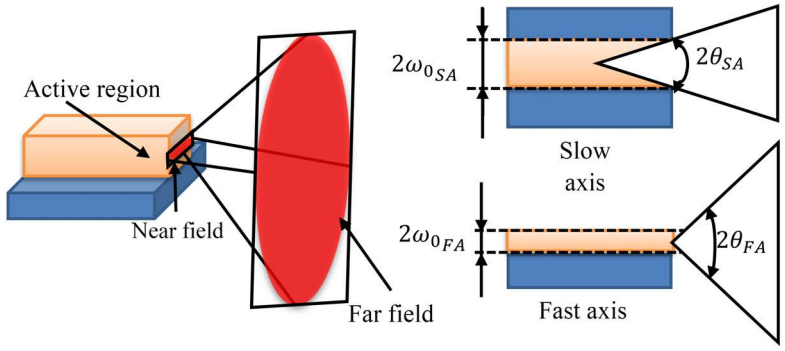

Fig. 4.1 Typical emitted beam from a laser chip and definition of NF and FF parameters.

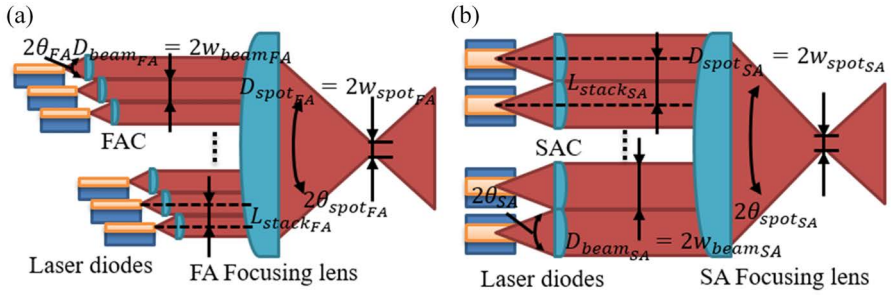

Fig. 4.2 Schematic representation of the LDs arrangement along (a) the FA and (b) the SA.

4. All the lenses are aberration-free.

5. The NA of each lens is equal to 1, so there is no truncation and even the marginal part of the beam can be well collimated or focused.

6. Laser diodes are arranged at a fixed interval along the FA and placed linearly along the SA as reported in Fig. 4.2. Besides for the vertical stacking, LDs arranging along the FA also introduces a longitudinal offset, which is necessary for the practical implementation of the multi-emitters but does not impact on the model derivation.

It is well known that the beams emitted from LDs are not exactly Gaussian shaped; nevertheless, they can be analyzed with the same formalism by introducing the M^2 factor approximation as mentioned in Sec. 2.2. Consider Fig. 4.2(a) as an example. Since the EFL of the collimating lens (both FA and SA) is greater than the Rayleigh range, the beam waist after the FAC can be approximated as

$$w_{\text{beam}_{\text{FA}}}(f_{\text{FAC}}) \approx \frac{M_{\text{FA}}^2 \lambda}{\pi w_{0\text{FA}}} f_{\text{FAC}} = \theta_{\text{FA}} f_{\text{FAC}} \tag{4.1}$$

where f_{FAC} is the EFL of the FAC, M^2_{FA} is the FA M^2 factor and θ_{FA} is the FA beam divergence.

After being collimated, the beam passes through a focusing lens and concentrates on the focal plane. The spot size at this position is

$$w_{\mathrm{spot_{FA}}}(f_{\mathrm{foc_{FA}}}) = \frac{M^2_{\mathrm{FA}}\lambda}{\pi\omega_{\mathrm{beam_{FA}}}(f_{\mathrm{foc_{FA}}})} f_{\mathrm{foc_{FA}}} \tag{4.2}$$

where $w_{\mathrm{beam_{FA}}}$ is the beam waist at the entrance of the lens and $f_{\mathrm{foc_{FA}}}$ is the EFL of the FA focusing lens.

Given the assumption that the divergence of the collimated beam is negligible and the beam waist radius is constant after collimation, by substituting Eq. 4.1 into Eq. 4.2:

$$w_{\mathrm{spot_{FA}}}(f_{\mathrm{foc_{FA}}}, f_{\mathrm{FAC}}) = \frac{\mathrm{BPP_{FA}}}{\theta_{\mathrm{FA}}} \frac{f_{\mathrm{foc_{FA}}}}{f_{\mathrm{FAC}}} = w_{0\mathrm{FA}} \frac{f_{\mathrm{foc_{FA}}}}{f_{\mathrm{FAC}}} \tag{4.3}$$

where $\mathrm{BPP_{FA}}$ is the BPP of the FA, having used the definition of BPP, which is $\mathrm{BPP} = w_0\theta = M^2\lambda/\pi$.

As evident from Fig. 4.2(a), each beam can be truncated by nearby lenses and possibly limited by the focusing lens clear aperture, if this is not large enough. Consequently, some power is lost by the truncation, but this is not considered in the model since the stack height is usually designed to be much greater than twice the beam radius at $1/\mathrm{e}^2$ intensity. In any case, even if each beam were truncated at $1/\mathrm{e}^2$ intensity of the beam waist, the power loss would be less than 3% (this aspect will be discussed in the last section). On the focal plane the spot size of a N diodes stack is the same as the spot size of a single diode; this proof can be found in Appendix A.

If N collimated beams overlap at the waist of $1/\mathrm{e}^2$ intensity, the divergence (half angle) of N focused beam is:

$$\theta_{\mathrm{foc}\,\mathrm{FA}} = N\frac{w_{\mathrm{beam_{FA}}}(f_{\mathrm{FAC}})}{f_{\mathrm{foc_{FA}}}} = N\frac{\theta_{\mathrm{FA}} f_{\mathrm{FAC}}}{f_{\mathrm{foc_{FA}}}} \tag{4.4}$$

Since the distance between two adjacent chips may be not equal to the beam waist, Eq. 4.4 must be modified, yielding:

$$\theta_{\mathrm{foc}\,\mathrm{FA}} = \left(\frac{N-1}{2} L_{\mathrm{stack_{FA}}} + \theta_{\mathrm{FA}} f_{\mathrm{FAC}}\right) / f_{\mathrm{foc_{FA}}} \tag{4.5}$$

where $L_{\text{stack}_{\text{FA}}}$ is the distance between two adjacent chips.

This result can be extended to Fig. 4.2(b). Assuming that a module includes N_{FA} LDs along the FA and N_{SA} diodes along the SA, the diagonal beam waist on the focal plane will be:

$$w_{\text{dia}} = \sqrt{(w_{0\text{FA}}\frac{f_{\text{foc}_{\text{FA}}}}{f_{\text{FAC}}})^2 + (w_{0\text{SA}}\frac{f_{\text{foc}_{\text{SA}}}}{f_{\text{SAC}}})^2} \tag{4.6}$$

where $f_{\text{foc}_{\text{FA}}}$, f_{FAC}, $f_{\text{foc}_{\text{SA}}}$ and f_{SAC} are the EFL of the FA focusing lens, of the FAC, of the SA focusing lens, and of the SAC, respectively.

Similar to the diagonal beam waist, the divergence of the focused beam is

$$\theta_{\text{dia}} = \sqrt{(\frac{\frac{N_{\text{FA}}-1}{2}L_{\text{stack}_{\text{FA}}} + \theta_{\text{FA}}f_{\text{FAC}}}{f_{\text{foc}_{\text{FA}}}})^2 + (\frac{\frac{N_{\text{SA}}-1}{2}L_{\text{stack}_{\text{SA}}} + \theta_{\text{SA}}f_{\text{SAC}}}{f_{\text{foc}_{\text{SA}}}})^2} \tag{4.7}$$

Then, multiplying Eq. 4.6 and Eq. 4.7, the diagonal BPP is given by

$$\begin{aligned}\text{BPP}_{\text{dia}} = &\left(\left(\frac{w_{0\text{FA}}}{f_{\text{FAC}}}\frac{N_{\text{FA}}-1}{2}L_{\text{stack}_{\text{FA}}} + w_{0\text{FA}}\theta_{\text{FA}}\right)^2\right.\\ &+\left(\frac{w_{0\text{SA}}}{f_{\text{SAC}}}\frac{N_{\text{SA}}-1}{2}L_{\text{stack}_{\text{SA}}} + w_{0\text{SA}}\theta_{\text{SA}}\right)^2\\ &+\left(w_{0\text{FA}}\frac{f_{\text{foc}_{\text{FA}}}}{f_{\text{foc}_{\text{SA}}}}\left(\frac{N_{\text{SA}}-1}{2}\frac{L_{\text{stack}_{\text{SA}}}}{f_{\text{FAC}}} + \frac{f_{\text{SAC}}}{f_{\text{FAC}}}\theta_{\text{SA}}\right)\right)^2\\ &\left.+\left(w_{0\text{SA}}\frac{f_{\text{foc}_{\text{SA}}}}{f_{\text{foc}_{\text{FA}}}}\left(\frac{N_{\text{FA}}-1}{2}\frac{L_{\text{stack}_{\text{FA}}}}{f_{\text{SAC}}} + \frac{f_{\text{FAC}}}{f_{\text{SAC}}}\theta_{\text{FA}}\right)\right)^2\right)^{1/2}\end{aligned} \tag{4.8}$$

If all collimated beams are arranged at the waist of $1/e^2$ intensity, Eq. 4.8 becomes:

$$\begin{aligned}\text{BPP}_{\text{dia}} =&((N_{\text{FA}}\text{BPP}_{\text{FA}})^2 + (N_{\text{FA}}\text{BPP}_{\text{SA}}\frac{\theta_{\text{FA}}f_{\text{FAC}}f_{\text{foc}_{\text{SA}}}}{\theta_{\text{SA}}f_{\text{SAC}}f_{\text{foc}_{\text{FA}}}})\\ &+(N_{\text{SA}}\text{BPP}_{\text{SA}})^2 + (N_{\text{SA}}\text{BPP}_{\text{FA}}\frac{\theta_{\text{SA}}f_{\text{SAC}}f_{\text{foc}_{\text{FA}}}}{\theta_{\text{FA}}f_{\text{FAC}}f_{\text{foc}_{\text{SA}}}}))^{1/2}\end{aligned} \tag{4.9}$$

Let:

$$\begin{aligned} A &= \left(N_{\mathrm{FA}} \mathrm{BPP}_{\mathrm{SA}} \frac{\theta_{\mathrm{FA}} f_{\mathrm{FAC}}}{\theta_{\mathrm{SA}} f_{\mathrm{SAC}}} \right)^2 \\ B &= \left(N_{\mathrm{SA}} \mathrm{BPP}_{\mathrm{FA}} \frac{\theta_{\mathrm{SA}} f_{\mathrm{SAC}}}{\theta_{\mathrm{FA}} f_{\mathrm{FAC}}} \right)^2 \\ c &= \left(\frac{f_{\mathrm{foc}_{\mathrm{SA}}}}{f_{\mathrm{foc}_{\mathrm{FA}}}} \right)^2 \\ g(c) &= \mathrm{BPP}_{\mathrm{dia}}^2. \end{aligned}$$

Squaring both sides of Eq. 4.9 and then substituting A, B and c in it

$$\begin{aligned} g(c) &= \mathrm{BPP}_{\mathrm{dia}}^2 \\ &= (N_{\mathrm{FA}} \mathrm{BPP}_{\mathrm{FA}})^2 + (N_{\mathrm{SA}} \mathrm{BPP}_{\mathrm{SA}})^2 + Ac + B\frac{1}{c}. \end{aligned} \tag{4.10}$$

It is easy to show that

$$\begin{aligned} g(c) \geqslant & (N_{\mathrm{FA}} \mathrm{BPP}_{\mathrm{FA}})^2 + (N_{\mathrm{SA}} \mathrm{BPP}_{\mathrm{SA}})^2 + 2\sqrt{AB} = \\ &= (N_{\mathrm{FA}} \mathrm{BPP}_{\mathrm{FA}} + N_{\mathrm{SA}} \mathrm{BPP}_{\mathrm{SA}})^2, \end{aligned}$$

where the equality holds if and only if $c = \sqrt{B/A}$. Therefore the minimum of $g(c)$ is $(N_{\mathrm{FA}} \mathrm{BPP}_{\mathrm{FA}} + N_{\mathrm{SA}} \mathrm{BPP}_{\mathrm{SA}})^2$, which for $N_{\mathrm{FA}} = N_{\mathrm{SA}} = 1$ gives Eq. 1.2.

4.2 Model Verification

The model has been validated with two different experiments. First, only one chip has been used to mimic the behavior of the multi-emitter stack; this method is simple, low cost and fast, but provides only a rough estimation of the coupling efficiency. Therefore, following the encouraging results obtained with the previous method, a full multi-emitter test module has been built and measured, obtaining an experimental validation not only the predicted BPP but also for the coupling efficiency.

4.2.1 Single Chip Setup

The actual multi-emitter configuration has been mimicked using the configuration sketched in Fig. 4.3, in which a single diode is moved at different positions reproduc-

ing the actual positions inside the multi-emitter package and then the various images are digitally superimposed.

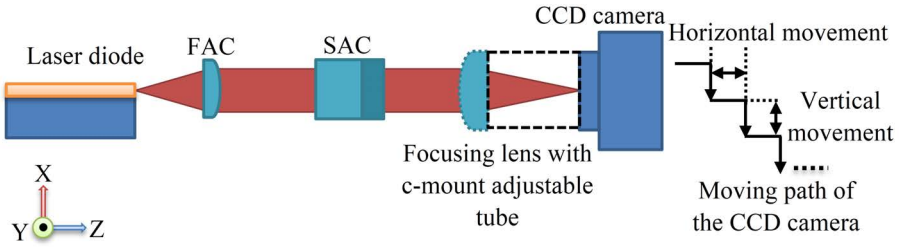

Fig. 4.3 Approach to emulate the stacking a plurality of diode laser chips by using a single LD.

In more detail, the approach can be divided into 7 steps:

1. Fix the FAC.
2. Adjust the SAC and the LD until the beam is well collimated.
3. Change the position of focusing lens so that the focal plane locates on the CCD exactly.
4. Move the CCD camera (which is mounted on a sub-micrometric 3-axis micro-positioner) along the edge of the staircase defining the spatial stacking up to the position of the n-th diode chip and shoot at the beginning of each step to acquire the image of in the focal plane.
5. Remove the focusing lens and move the CCD camera to the position of the front surface of the focusing lens and shoot to acquire the image of the n-th diode chip at the entrance of the focusing lens.
6. Repeat 4th and 5th steps for the desired number of chips to be combined.
7. Combine all the images into two images using a data processing software (Matlab^{TM} in our case): one image is for the beam at the entrance of the focusing lens and the other for the spot on the focal plane.
8. Calculate the characteristic parameters of the combined beam using an approach similar to that previously used for the analysis of the single images.

The comparison of the results obtained combining 6 chips using two FAC lenses, namely one with EFL = 600 µm and another with EFL = 1100 µm, is shown in Fig. 4.4. The horizontal movement used in both cases is 4 mm, whereas a 460 µm vertical movement is used for the 1100 µm EFL FAC experiment and a 850 µm vertical movement is adopted for the 600 µm EFL FAC experiment.

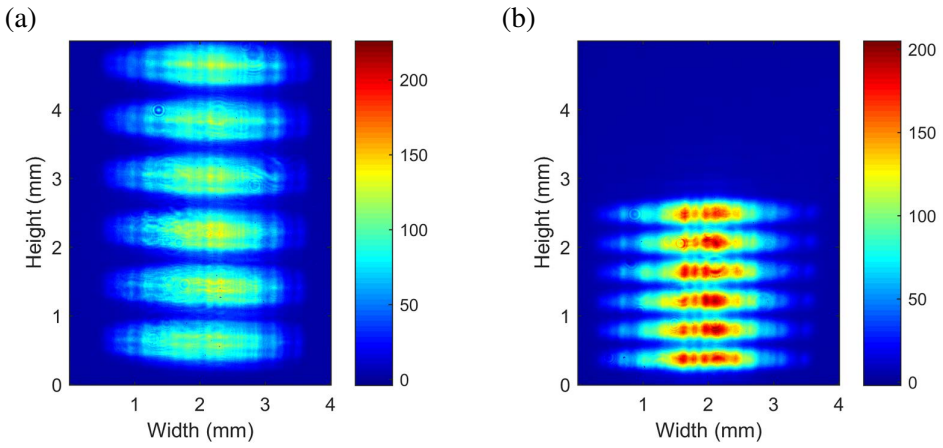

Fig. 4.4 Comparison of the images at the entrance of the focusing lens for the combination of 6 chips: (a) 1100 µm EFL FAC, and (b) 600 µm EFL FAC.

Using the shorter focal length FAC it is possible to further increase the number of combined chips for a fixed aperture: for instance, Fig. 4.5 shows an example with 10 chips. However, decreasing the size of the beam means increasing the divergence of the beam. Furthermore, the closer a LD to the CCD camera, the smaller its beam size. Therefore, it is obvious that in Fig. 4.4 the top beam shape is nearly identical to the bottom beam shape for case (a), while the beams exhibit some degradations for case (b). This phenomena tends to be more serious when an even shorter EFL FAC is used, a problem discussed in the next section.

An example of the impact of different focusing lenses is shown in Fig. 4.6, where three lenses are compared, with EFL = 100.1 mm, EFL = 49.8 mm and EFL = 8 mm, respectively. The measurements indicate that the spot shrinks when the EFL of the focusing lens decreases.

The experimental results are compared with theoretical predictions in Tab. 4.2 and Tab. 4.3 for the stacking of 10 and 6 LDs, respectively. Tab. 4.1 shows that both the number of LDs and the EFL of collimator have an impact on the total beam width. If the number of LDs or the EFL of collimator increases, the total beam expands.

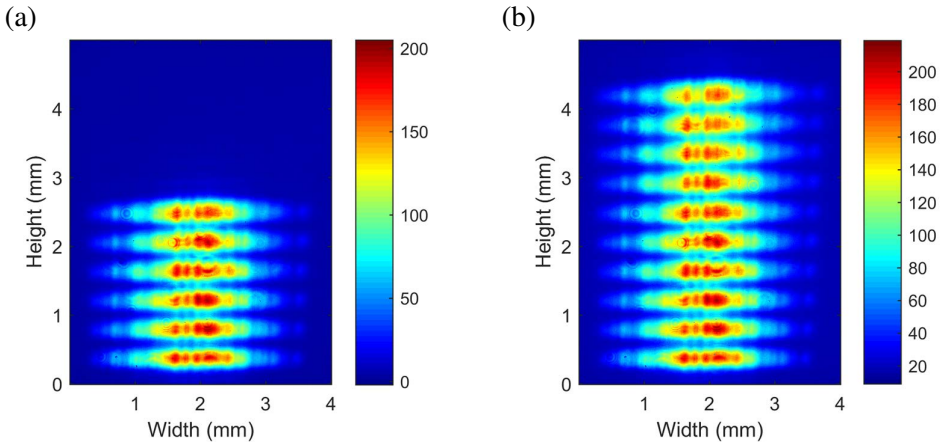

Fig. 4.5 Comparison of the images at the entrance of the focusing lens using a 600 µm EFL FAC: (a) combination of 6 chips and (b) combination of 10 chips.

Table 4.1 Comparison between measurements and calculations for combined beams using different FACs.

Item	Measurement	Calculation	Error
Beam FA width[a] (µm)	5271.2	5253.0	0.3%
Beam SA width[a] (µm)	2706.0	2764.6	2.1%
Beam FA width[b] (µm)	2899.6	2865.0	1.2%
Beam SA width[b] (µm)	2789.6	2764.6	4.6%
Beam FA width[c] (µm)	4800.4	4775.0	0.5%
Beam SA width[c] (µm)	2820.4	2764.6	2%

[a]Six combined beams with FAC of EFL 1100 mm. [b]Six combined beams with FAC of EFL 600 mm. [c]Ten combined beams with FAC of EFL 600 mm.

The result in Fig. 4.6 and in Tab. 4.4 demonstrate that the focusing spot at focal plane is the same for both the 10 and the 6 diodes cases.

The quite large error (13%) between measurements and calculations in the spot FA width for the EFL =8 mm focusing lens in Tab. 4.2 can be ascribed to the CCD camera resolution, which is limited to 4.4 µm. In practice, this means that, when the measured spot width is 8.8 µm to 13.2 µm range, the camera always returns 13.2 µm. Unfortunately, the actual spot FA width is equal to 11.6 µm, which is in the 8.8 to 13.2 µm range.

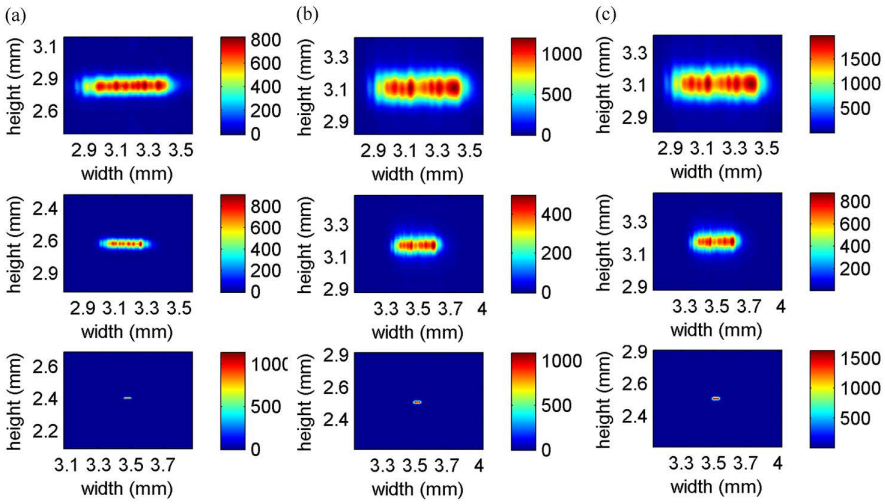

Fig. 4.6 Visual comparison of the impact of the focusing lens for the combination beams using different FACs and 12 mm EFL SAC. The first column is for a focusing lens with EFL = 100.1 mm, the second for a lens with EFL = 49.8 mm and the third for a lens with EFL = 8 mm.

4.2.2 Multi-emitter module

The experimental results above are obtained from one chip stack mimicking, which can be used to validate the BPP but not the predictions on the actual power fraction in different NAs from a fiber, not to mention the power loss due to stack blocking. Hence, three modules with 450 µm stack height and different number of chips (7, 8 and 9) have been built and measured. All the modules use 300 µm EFL FAC. The results are shown in Tab. 4.5. The used FAC EFL is the most challenging because the errors for 300 µm EFL FAC are larger than those obtainable using 600 µm or 1100 µm EFL FAC. This is because one of the assumptions is that the divergence of the collimated beam is negligible, which cannot be true for short EFL FAC.

For the 7 chip module the target is to obtain more than 99% of coupling efficiency in a 105 µm core fiber and more than 95% of the power in NA=0.15. Tab. 4.6 reports the coupling efficiency for 7 chips at 8 A from a power supply system that can turn on and off each channel separately. Fig. 4.7 shows a photo taken when all the chips are powered on before mounting the optical components. There are three factors that contribute to the loss of coupling efficiency:

1. the transmission of the optical components is not 100%;
2. part of tail of each beam is not focused into the fiber;

Table 4.2 Comparison between measurements and calculations for 6 combined beams using a 1100 µm EFL FAC.

Item	Measurement	Calculation	Error
Spot FA width[a] (µm)	154.0	145.4	5.9%
Spot SA width[a] (µm)	726.0	777.5	6.6%
BPP[a] (mm mrad)	11.0	11.7	6.1%
Spot FA width[b] (µm)	79.2	72.7	8.9%
Spot SA width[b] (µm)	376.2	388.7	3.2%
BPP[b] (mm mrad)	11.4	11.7	2.6%
Spot FA width[c] (µm)	13.2	11.6	13.8%
Spot SA width[c] (µm)	61.6	62.2	1.0%
BPP[c] (mm mrad)	11.7	11.7	0.3%

[a]Focusing lens of EFL = 100.1 mm. [b]Focusing lens of EFL = 49.8 mm. [c]Focusing lens of EFL = 8 mm.

3. some chips may have little misalignment.

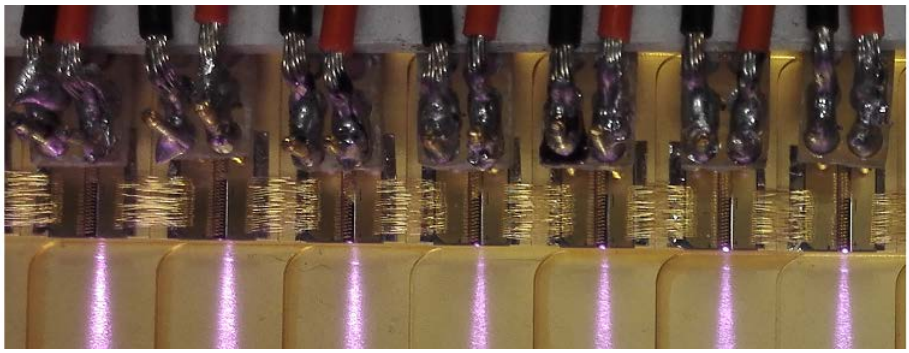

Fig. 4.7 Turning on all channels.

Fig. 4.8 shows the power fraction in different NAs at 12 A. The 7 chip module emits more than 76 W at 12 A from the fiber and the power in NA=0.15 is around 95%.

4.3 Application Example

This section describes an example on how to choose the right optical components to couple as many chips as possible to a 105 µm core, 0.22 NA fiber with 99% of

Table 4.3 Comparison between measurements and calculations for 6 combined beams using a 600 µm EFL FAC.

Item	Measurement	Calculation	Error
Spot FA width[a] (µm)	277.2	266.7	3.9%
Spot SA width[a] (µm)	734.8	777.5	5.5%
BPP[a] (mm mrad)	7.9	8.2	3.8%
Spot FA width[b] (µm)	140.8	133.3	5.6%
Spot SA width[b] (µm)	374.0	388.8	3.8%
BPP[b] (mm mrad)	8.1	8.2	1.6%
Spot FA width[c] (µm)	22.0	21.3	3.3%
Spot SA width[c] (µm)	61.6	62.2	1.0%
BPP[c] (mm mrad)	8.2	8.2	0.3%

[a]Focusing lens of EFL = 100.1 mm. [b]Focusing lens of EFL = 49.8 mm. [c]Focusing lens of EFL = 8 mm.

the within power NA = 0.17. The design requires choosing four optical elements, namely FAC, SAC, FA focusing lens and SA focusing lens, taking into account the constrains in selecting those optical components. For instance, the EFL of FAC in the market ranges from a few hundred micron to a few millimeter [44, 45]; since customized FACs are very expensive especially for low production volumes, the choice is practically obliged to fall on an off-the-shelf product.

Assume that the constrains are:

1. Preferential FAC has EFL =300 µm.
2. The stack height is 500 µm.
3. There is only one chip along the SA direction, so that $N_{SA} = 1$. If two chips are arranged along the SA direction, the minimal diagonal BPP will be larger than the BPP of the fiber even there is only one chip along the FA direction.
4. The chip has 1.60 µm FA full width, 44° FA full divergence angle, 94 µm SA full width and 10° SA full divergence angle.

Table 4.4 Comparison between measurements and calculations for 10 combined beams using a 600 µm EFL FAC.

Item	Measurement	Calculation	Error
Spot FA width[a] (µm)	277.2	266.7	3.9%
Spot SA width[a] (µm)	734.8	777.5	5.5%
BPP[a] (mm mrad)	10.9	11.3	3.4%
Spot FA width[b] (µm)	140.8	133.3	5.6%
Spot SA width[b] (µm)	374.0	388.8	3.8%
BPP[b] (mm mrad)	11.2	11.3	1.2%
Spot FA width[c] (µm)	22.0	21.3	3.3%
Spot SA width[c] (µm)	61.6	62.2	1.0%
BPP[c] (mm mrad)	11.4	11.3	0.7%

[a]Focusing lens of EFL = 100.1 mm. [b]Focusing lens of EFL = 49.8 mm. [c]Focusing lens of EFL = 8 mm.

Table 4.5 Comparison between measurements and calculations for actual multi-emitter modules with different number of chips.

Items	Measurement	Calculation	Error
BPP[a] (mm mrad)	8.2	8.6	4.9%
BPP[b] (mm mrad)	9.1	9.7	6.6%
BPP[c] (mm mrad)	10.1	10.7	5.9%

[a]7 chips. [b]8 chips. [c]10 chips.

Upon substitution of these values in Eq. 4.8, the equation becomes

$$\mathrm{BPP_{dia}} = \left((0.67 \times (N_{\mathrm{FA}} - 1) + 0.31)^2 + 15.42 + \left(2.33 \times 10^{-4} \times \frac{f_{\mathrm{foc_{FA}}} f_{\mathrm{SAC}}}{f_{\mathrm{foc_{SA}}}} \right)^2 + \left(\frac{f_{\mathrm{foc_{SA}}}}{f_{\mathrm{foc_{FA}}} f_{\mathrm{SAC}}} \left(1.13 \times 10^4 \times (N_{\mathrm{FA}} - 1) + 5.18 \times 10^3 \right) \right)^2 \right)^{1/2} \tag{4.11}$$

Table 4.6 Coupling efficiency for each of the 7 chip module.

Chip index	1	2	3	4	5	6	7
Coupling efficiency (%)	94.0	95.6	92.0	93.0	94.8	92.1	93.8

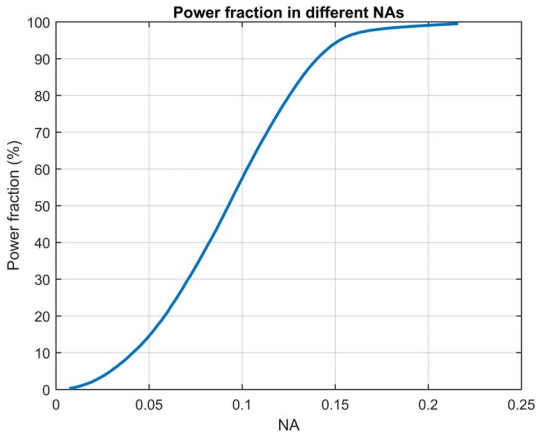

Fig. 4.8 Power fraction in different NAs.

Let

$$\begin{aligned} A =& N_{\mathrm{FA}} - 1 \\ B =& \frac{f_{\mathrm{foc_{FA}}}}{f_{\mathrm{foc_{SA}}}} f_{\mathrm{SAC}} \\ f(A,B) =& \mathrm{BPP}_{\mathrm{dia}}^2. \end{aligned}$$

In order to simplify the computation, squaring both sides of Eq. 4.11 and then substituting A, B and $f(A,B)$ in it:

$$\begin{aligned} f(A,B) =& (0.67 \times A + 0.31)^2 + 15.42 + 5.42 \times 10^{-8} \times B^2 \\ &+ \frac{1}{B^2}(1.13 \times 10^4 \times A + 5.18 \times 10^3)^2 \end{aligned} \tag{4.12}$$

Taking the first order partial derivatives of $f(A,B)$ with respect to A and B,

$$\begin{aligned} \frac{\partial f}{\partial A} =& 1.34 \times (0.67 \times A + 0.31) + \frac{2.36 \times 10^4}{B^2}(1.18 \times 10^4 \times A + 5.41 \times 10^3) \\ \frac{\partial f}{\partial B} =& 1.09 \times 10^{-7} \times B - \frac{2}{B^3}(1.13 \times 10^4 \times A + 5.18 \times 10^3)^2 \end{aligned} \tag{4.13}$$

It is obvious that the partial derivative with respect to A will be always greater than 0. This indicates that $f(A,B)$ increases with the number of chips and that the maximum number of chips that can be coupled into a fiber is fixed no matter how optical components change. However, the partial derivative with respect to B tends to be zero when $B = \sqrt{5.05 \times 10^7 \times A + 2.37 \times 10^7}$. This implies that for a given A, there

is always an optimum combination of optical components making $f(A,B)$ minimum, which coincides to the assert that the BPP is an optical invariant and it cannot be improved by passive optical systems. Substituting $B = \sqrt{4.84 \times 10^7 \times A + 2.22 \times 10^7}$ to Eq. 4.12 gives:

$$f(A) = 0.45 \times A^2 + 5.66 \times A + 17.92 \tag{4.14}$$

The BPP of the fiber is 8.93 mm mrad, so Eq. 4.14 cannot exceed the square of this number and this gives a maximum for A of 6. Then, the value of B is equal to 17.68 mm. On the one hand, the small diagonal BPP allows improving the module performance; on the other hand, a small package is preferred. Hence, within the possible solutions, a shorter EFL SAC is preferable. Fixing A to 6, then Eq. 4.12 becomes:

$$f(B) = 34.17 + 5.42 \times 10^{-8} \times B^2 + \frac{5.33 \times 10^6}{B^2} \tag{4.15}$$

The plot of Eq. 4.15 is reported in Fig. 4.9; the abscissae are limited to the use of 11.4 mm EFL focusing lens so that w_{dia} and θ_{dia} fit the core and the NA constrain, respectively. Clearly, the best EFL for the SAC is about 12 mm, which makes BPP_{dia} small enough and keeps the package compact.

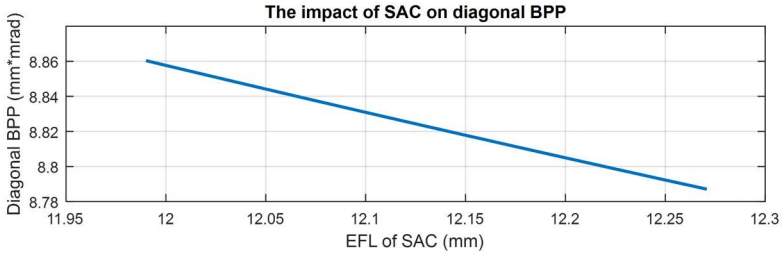

Fig. 4.9 The impact of SAC on diagonal BPP.

4.4 Power Loss Analysis in Fiber Coupled Module

Both optical components and design contribute to the power loss in multi-emitter fiber coupled modules; the latter, however, plays a more important role because losses introduced by optics cannot be improved greatly as the optics with even higher quality costs more and/or requests very strict application environment. In contrast, sophisticated design not only minimizes the power loss, but also allows improving the package footprint and overall performance. Power loss is an issue not only by

itself, but also because the lost power contributes to increse the temperature and/or can damage some components.

4.4.1 Optical Components

The loss introduced by optical components has three contributions: transmission from HR coatings, reflection from AR coatings and absorption in the bulk material. With reference to Fig. 1.8, first the FACs collimate the beams from each chip in the FA direction; next the SACs collimate partially collimated beams in the SA direction. Then, the mirrors bend well-collimated beams by 90° and, finally, the focusing lens couples the stacked beams in to the fiber. FAC, SAC, focusing lens and fiber ferrule have AR coatings and mirrors have HR coatings. However, even if AR or HR coatings are deposited on high quality optical substrates, their transmittance or reflectance cannot be 100%, as shown in Fig. 4.10 for a commercial device [46]. The total loss caused by these coatings can be estimated to be at least 3%. As for the absorption of FACs, SACs and focusing lenses, if all the lenses are made by optical glass, the contribution to overall power loss will be less than 0.02%, which is negligible.

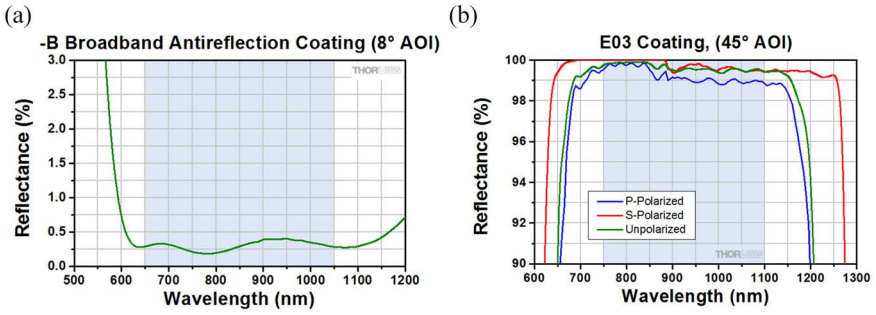

Fig. 4.10 Typical performance of (a) AR and (b) HR coatings.

4.4.2 Design

The estimation of loss caused by the design is more complicated. To start with, there is a trade-off between the requirement of coupling as much as possible power into the fiber and that of making the package as compact as possible. Indeed, to reduce the package occupation it is necessary to truncate part of beam. To simplify the

explanation, it can be assumed that the beams have exactly Gaussian shape and are arranged in only the FA direction. Three simulations were performed to investigate how truncation affects the power loss, as shown in Fig. 4.11, 4.13 and 4.14. In all these cases the beam intensity distribution at the entrance of the lens on the focal plane and compare it with simulations done considering infinite aperture.

In the first example, the distance of two adjacent collimated beams is equal to full width at half maximum of the collimated beam, so that $L_{\text{stackFA}} = \theta f_{\text{FAC}} \sqrt{2ln(2)}$, where θ is the divergence along the FA. By substituting the parameters of Chip E measured in Ch. 3 into the expression for L_{stackFA} and Eq. 4.8, it is found L_{stackFA} =0.14 mm and the maximal number of chips N_{FA} that can be coupled into a 0.22NA, 105 µm core multimode optical fiber is 33. However, the power loss due to truncation, which can be clear seen in Fig. 4.11(a) in which left and right sides are cut, is

$$100\% - \frac{\int_0^{0.59\omega_0} \exp(-2x^2/w_0^2)dx}{\int_0^{+\infty} \exp(-2x^2/w_0^2)dx} \cdot 100\% = 26\%$$

Furthermore, the beam profile enlarges seriously on the focal plane as shown in Fig. 4.11(b), so that the beam width becomes much wider and cannot be coupled into the fiber. Fig. 4.12 shows also that the truncation not only makes the beam wider, but also generates side lobes. Let a be the unaffected beam radius, the power of truncated beam in the range $(-a,+a)$ is $\frac{\int_0^a I(x)dx}{\int_0^{+\infty} I(x)dx} \times 100\% = 66\%$. So the total power loss will be more than half, 52%. Assuming that each chip emits 10 W, the output without considering the loss from coating is 161 W instead of the theoretic maximum of 330 W.

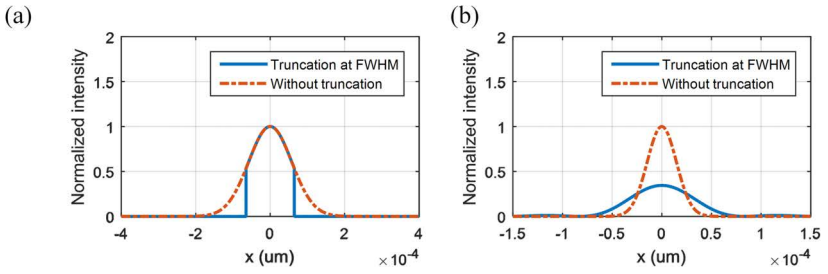

Fig. 4.11 The intensity distribution of the beam truncated at the half maximum: (a) at the entrance of 11 mm EFL lens, and (b) on the focal plane.

The second example considers that each beam is truncated at $1/e^2$ intensity, which changes L_{stackFA} to 0.24 mm and N_{FA} is to 19. Compared to Fig. 4.11(a), it is

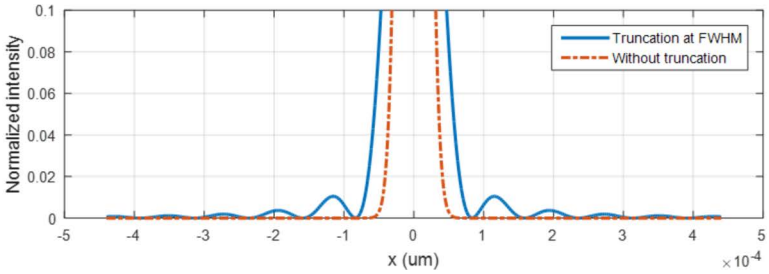

Fig. 4.12 Zoom in of Fig. 4.11(b).

obvious that the truncation in Fig. 4.13(a) is much less. The corresponding power loss can be calculated by using the same equation, obtaining 6%. In the meanwhile, the beam profile on the focal plane has not evident side lobes as shown in Fig. 4.13(b). The power contained in the $(-a, +a)$ range is 95%, so the output in this case will be 169 W.

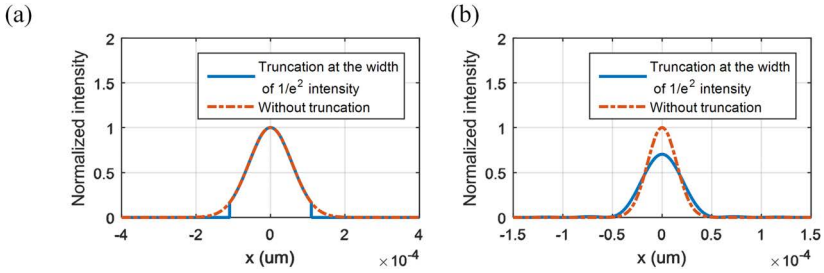

Fig. 4.13 Intensity distribution of the beam truncated at $1/e^2$ intensity: (a) at the entrance of 11 mm EFL lens, and (b) on the focal plane.

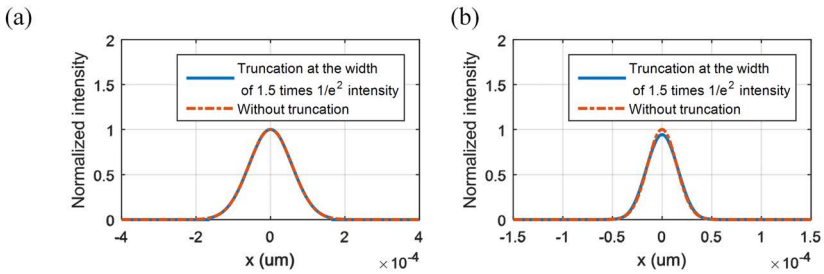

Fig. 4.14 The intensity distribution of the beam truncated at 1.5 times the width of $1/e^2$ intensity: (a) at the entrance of 11 mm EFL lens, and (b) on the focal plane.

The last example considers truncating the beam at 1.5 times the width of $1/e^2$ intensity; this yields to negligible power loss (0.5%) and a very good beam intensity distribution: 98% power in the $(-a, +a)$ range, which is almost the same as the

beam profile without truncation, as shown in Fig. 4.14(b), but N_{FA} reduces to 13. The final coupled power is 127 W.

As a general conclusion that can be drawn from the previous three examples, strong truncation configurations cause the focused spot size increasing problem, the weak truncation configurations make the spot size larger but acceptable since only a few percent of power is out of the range $(-a,+a)$, and the further enlarging of L_{stackFA} does not increase the spot size but leads to a lower number of chips that can be coupled. In a word, two adjacent beams cannot be neither too close nor too far apart.

Chapter 5

Optical Components Assembly

The most difficult assembly procedure for the optical devices composing the multi-emitter module is for mounting the FAC. Indeed, considering the 300 µm EFL FAC as an example, its BFL is only 70 µm; as the beam rapidly diverges, the tolerance for positioning the FAC along the optical axis is about 500 nm. This, combined with angular misalignment sensitivity, makes the FAC assembly extremely sensitive to movements and thus critical, so the focus of this chapter will be on the development of an efficient approach to assemble the FACs.

5.1 Introduction to FAC Assembling

The multi-emitter module assembly requires a large number of steps because of its complexity in terms of optics alignment, especially for the FAC. During the process definition or for special modules, the alignments require the manual intervention of skilled technicians. Once the assembly procedure is well established, it is possible to automated it using specific machines [47]; nevertheless, it is a quite long process, that can last between one to two hours depending on the number of elements (strictly related to the number of chips, hence of the output power) and the efficiency of the alignment algorithms.

In practice, a FAC, which is an acylindrical lens with large NA [48], must always be used to collimate the emitted beam from each chip in the FA direction, as shown in Fig. 5.1, because LDs exhibit a large divergence angle in this FA direction, as already mentioned in Ch. 1. Commercial FACs have typically EFL ranging from

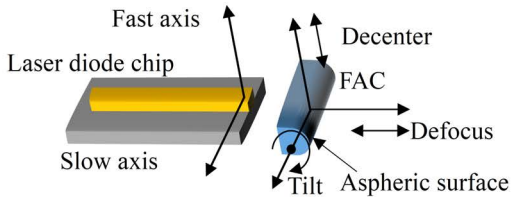

Fig. 5.1 Schematic representation of a LD chip with the lens used to collimate the emitted beam along the FA direction and identification of the tilt, decenter and defocus parameters.

few hundreds of micrometers to few millimeters: on the one hand, a short EFL allows a much more compact layout (a largely sought characteristics especially for high power modules that include many chips); on the other hand, short EFL values make handling more difficult since the resulting collimated beam is more sensitive to tilt, decenter and defocus. In this chapter, tilt denotes the tilt of FAC about the axis perpendicular to the FA; decenter the vertical offset with the respect to the semiconductor laser chip active region center; defocus the offset with respect to the position identified by the lens EFL (Fig. 5.1).

For instance, Fig. 5.2 compares the impact of 1° tilt, 2 µm decenter and 1 µm defocus on a 1100 µm EFL FAC with that on a 300 µm EFL FAC . It is clear that the peak position and the beam width of the 300 µm EFL FAC are more susceptible to misalignments. The light source used for both cases is a Gaussian beam at 920 nm wavelength, with beam waist of 1 µm and $1/e^2$ half divergence of 16.8°; the detector is placed 500 mm away from the source. At first glance the 1° tilted beam for the 300 µm EFL FAC seems the optimal result, in practice it is a working condition that should be avoided. Consider, as an example, a fiber-coupled multi-emitter module composed of 7 chips, 6 of which emit well collimated beams (i.e., perfect alignment) and 1 a 1 degree tilted beam; if the fiber has the right size and numerical aperture to couple 7 well collimated beams, it is possible to see that the 6 well collimated beam will actually be coupled into the fiber, but the tilted beam won't because it does not superpose to other beams on the focal plane and its beam waist is wider than the others.

Alignment errors in the FAC position, especially for short EFL values, can be reduced by actively aligning the lens using a high resolution camera; however, this is a complex operation that requires either experienced operators to properly relate the lens position and the measured field distribution on the detector or very efficient and "smart" automatic routines. In order to simplify the FAC assembly procedure, an

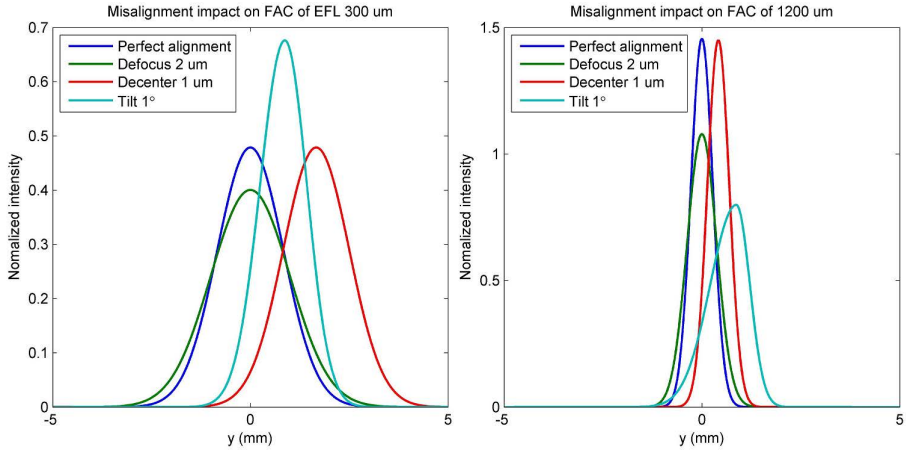

Fig. 5.2 Comparison of the impact of the same combination of tilt, decenter and defocus on two FACs with different EFLs: left picture for 300 µm EFL and right picture for 1200 µm EFL .

approach relying on a BP-ANN has been developed to assist the operators in finding the optimal lens position. The BP-ANN uses as input four parameters characterizing the beam as measured from the camera (namely, the peak position, the centroid position, the asymmetry and the width, as defined later in this chapter) and returns the tilt, the decenter and the defocus of the lens. The neural network has been trained using a Gaussian beam ray-equivalent model, which proved to be accurate enough for practical applications. Many papers [49–52] have already demonstrated setups and approaches for FAC automatic alignment, but most of them need fine pre-alignment and two cameras to monitor the NF and the FF distributions, and this increases the complexity and the cost of the system. In comparison, the proposed approach requires only one camera and coarse pre-alignment. Moreover, currently available optimization algorithms use several iterations to converge to the optimum position, requiring multiple movements and several seconds, while the proposed approach calculates directly the correct position and allows placing the lens in the correct position ideally in just two steps (in theory one step is enough and the reason why two steps are used will be explained in Sec.5.4), with clear advantages in terms of cycle time and lifetime of the aligning equipment. Using the proposed procedure, with manual pre-alignment, the time cost of FAC assembly is less than 1 minute. For comparison it should be pointed out that a commercial automatic equipment requires today from 30 s to 60 s; it is therefore expected that once the proposed BP-ANN approach were implemented in automatic assembly machine, the time

should be reduced to few seconds. Part of the results reported in this chapter have been published in [28] and in [43].

5.2 Constructing Data Set by Gaussian Beam Ray-equivalent Model

Key for the proposed approach is the construction of the data set used to train and preliminary test the BP-ANN. This starts with the creation of the chief ray, the waist rays and the divergence rays from the parameters characterizing the light source, as discussed in Ch. 2. Then, three steps are iterated for each orientation (in terms of tilt, decenter and defocus) of the FAC:

1. Trace the chief ray, the waist rays and the divergence rays and find their intersection with the detector.
2. Discretize the detector, apply Eq. 2.11 to the discrete set and determine the intensity distribution.
3. Calculate the peak position, the centroid position, the asymmetry and the $1/\mathrm{e}^2$ intensity width; save these values together with the defocus, the decenter and the tilt of the FAC.

The asymmetry of the profile is defined as:

$$\text{asymmetry} = \frac{\int_{\text{left } 1/\mathrm{e}^2 \text{ position}}^{\text{peak position}} I(x)\mathrm{d}x}{\int_{\text{peak position}}^{\text{right } 1/\mathrm{e}^2 \text{ position}} I(x)\mathrm{d}x}. \tag{5.1}$$

5.3 BP-ANN training with simulation results

This section illustrates how to build a BP-ANN and then the network training by using the simulation results obtained from the Gaussian beam ray-equivalent model.

5.3.1 Creation of the BP-ANN

The generation of a BP-ANN consists of two phases:

1. Forward propagation of training data through the input layer, the hidden layer and the output layer;

2. Backward propagation of forward errors.

The BP-ANN learning procedure repeatedly adjusts the weights of the connections in the network so as to minimize a measure of the difference between the actual output vector of the net and the desired output vector [53].

Fig. 5.3 reports the generic schematic layout of the type of BP-ANN used for FAC assembling assistance. In FAC assembling case the network is composed by $I = 4$ input neurons, $J = 20$ and $M = 40$ hidden neurons, and $N = 3$ output neurons, so there are four inputs, three outputs and two hidden layers. The four input variables represent, in order, the peak position, the centroid position, the asymmetry and the width; they are indicated with x_{p1}, x_{p2}, x_{p3} and x_{p4}, where p indicates the p-th sample and the total number of the training sample is P. Similarly the outputs are indicated with y_{p1}, y_{p2} and y_{p3} and are the tilt, the decenter and the defocus. The three targets are indicated with t_{p1}, t_{p2} and t_{p3}. Practical verifications have shown that two hidden layers is the minimum network complexity to map input variables into output targets with the required accuracy level.

The connection weights between the i-th neuron of the input layer and the j-th neuron of the first hidden layer, the j-th neuron of the first hidden layer and the m-th neuron of the second hidden layer, and the m-th neuron of the second hidden layer and the n-th neuron of the output layer are respectively indicated by w^1_{ij}, w^2_{jm} and w^3_{mn}. The outputs of the j-th neuron of the first hidden layer and of the m-th neuron of the second hidden layer are indicated by O^1_{pj} and O^2_{pm}, respectively.

The BP-ANN training requires the following steps:

1. Random initialization of all the weights and set of the training parameters: learning rate $\mu = 0.01$, the maximal iteration 5000, performance $\varepsilon = 0.01$, and loop indicator $k = 0$.

2. Normalization of the simulation results, dividing the simulation data into two groups, one for training and the other for testing.

3. Determination of weights: for each sample in the data set:

   (a) Calculate O^1_{pj}, O^2_{pm} and y_{pn} by applying:

$$O^1_{\mathrm{pj}}(k) = f\left(\sum_{\mathrm{i}=1}^{I} w^1_{\mathrm{ij}}(k) x_{\mathrm{pi}}\right), \tag{5.2}$$

$$O^2_{\mathrm{pm}}(k) = f\left(\sum_{\mathrm{j}=1}^{J} w^2_{\mathrm{jm}}(k) O^1_{\mathrm{pj}}(k)\right), \tag{5.3}$$

$$y_{\mathrm{pn}}(k) = f\left(\sum_{\mathrm{m}=1}^{M} w^3_{\mathrm{mn}}(k) O^2_{\mathrm{pm}}(k)\right), \tag{5.4}$$

   where $f(x)$ is the tangent sigmoid activation function: $2/(1+\mathrm{e}^{-2*x})-1$.

   (b) Compute the mean square error $E = \frac{1}{N}\sum_{\mathrm{n}=1}^{N}(t_{\mathrm{pn}} - y_{\mathrm{pn}}(k))^2$.

   (c) Update weights; compute correction factors first:

$$\Delta w^1_{\mathrm{ij}}(k+1) = \mu \sum_{\mathrm{p}=1}^{P} \delta_{\mathrm{pj}}(k) x_{\mathrm{pi}}, \tag{5.5}$$

$$\Delta w^2_{\mathrm{jm}}(k+1) = \mu \sum_{\mathrm{p}=1}^{P} \delta_{\mathrm{pm}}(k) O^1_{\mathrm{pj}}(k), \tag{5.6}$$

$$\Delta w^3_{\mathrm{mn}}(k+1) = \mu \sum_{\mathrm{p}=1}^{P} \delta_{\mathrm{pn}}(k) O^2_{\mathrm{pm}}(k), \tag{5.7}$$

   where

$$\delta_{\mathrm{pn}}(k) = (t_{\mathrm{pn}} - y_{\mathrm{pn}}(k)) y_{\mathrm{pn}}(k)(1 - y_{\mathrm{pn}}(k)),$$

$$\delta_{\mathrm{pm}}(k) = O^2_{\mathrm{pm}}(k)(1 - O^2_{\mathrm{pm}}(k)) \sum_{\mathrm{n}=1}^{N} \delta_{\mathrm{pn}}(k) w^3_{\mathrm{mn}}(k),$$

$$\delta_{\mathrm{pj}}(k) = O^1_{\mathrm{pj}}(k)(1 - O^1_{\mathrm{pj}}(k)) \sum_{\mathrm{m}=1}^{M} \delta_{\mathrm{pm}}(k) w^2_{\mathrm{jm}}(k);$$

then add the weight difference:

$$w_{ij}^{1}(k+1) = w_{ij}^{1}(k) + \Delta w_{ij}^{1}(k+1), \tag{5.8}$$

$$w_{jm}^{2}(k+1) = w_{jm}^{2}(k) + \Delta w_{jm}^{2}(k+1), \tag{5.9}$$

$$w_{mn}^{3}(k+1) = w_{mn}^{3}(k) + \Delta w_{mn}^{3}(k+1). \tag{5.10}$$

4. If the maximum value of E is less than or equal to ε or k is greater than the maximum number of iterations, then saving the network configuration and stopping; otherwise increasing k by 1 and starting again from step 3.

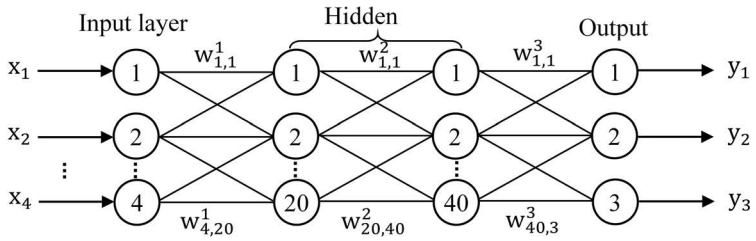

Fig. 5.3 Schematic map of the BP-ANN used for FAC assembling assistance.

5.3.2 Training results

Fig. 5.4 shows the layout considered to generate the training data for the neural network already constructed in the previous section. The parameters of Chip E reported in Ch. 3 are used for the training and test phases and four different EFL FACs, namely 200 µm, 300 µm, 600 µm and 1200 µm, are simulated. In each simulation, various cases, which are composed of the combination of different defocus, decenter and tilt, are considered. For example, the 300 µm EFL FAC simulation consists of 201 defocus values (from 0 µm to +60 µm, increments of 0.3 µm), 201 decenter values (from −30 µm to +30 µm, increments of 0.3 µm) and 133 tilt values (from −5° to +5°, increments of 0.075°). There are more than 5 million combinations, but not all of them are useful because the intensity in the detector is zero if the beam does not hit the detector. 17805 meaningful cases are obtained from the 300 µm

EFL FAC simulation, and then 10% of them are set apart to test the neural network, whereas the remaining 90% are used for the training phase. The training stopped upon reaching the maximum number of iterations. The performance parameter is 0.0056. The time cost of each simulation and training is less than 3 hours: this indicates that if a new EFL FAC, for instance 150 µm, and a new chip need to be assembled, about 5 hours (2 extra hours for characterizing the NF and FF of the chip) are enough to train the procedure.

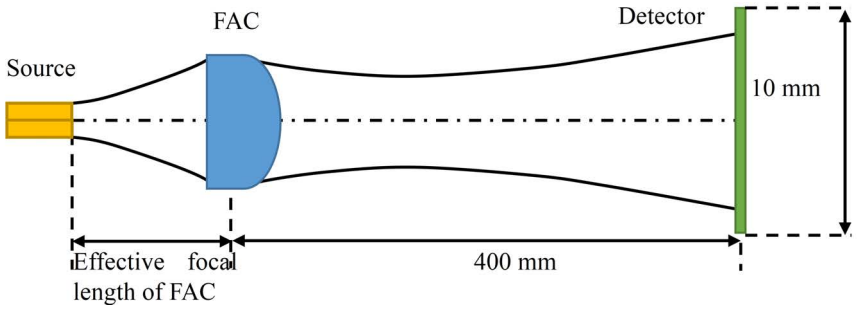

Fig. 5.4 Schematic of layout considered in training simulation.

The results obtained with the test set for a 300 µm EFL FAC are shown in Fig. 5.5 and demonstrate that, at the end of the training phase, the neural network is able to match very well the supplied target, especially for the decenter and tilt parameters. As for the defocus, there are many fluctuations in the range between 0 µm to 0.5 µm; therefore in practical experiments the control program introduces a fixed 0.5 µm compensation wherever the defocus indicated by the network is below than 0.5 µm .

5.4 Experimental validation of the proposed approach

5.4.1 Experimental setup

Fig. 5.6 shows the optical bench used to assemble the FACs, which uses some of the components already introduced for the benches used for the NF and FF characterization of the diode chips, such as high precision computer controlled 6-axis positioning stage and NIR cameras. From the experimental point of view, the assembly procedure can be divided into four main steps:

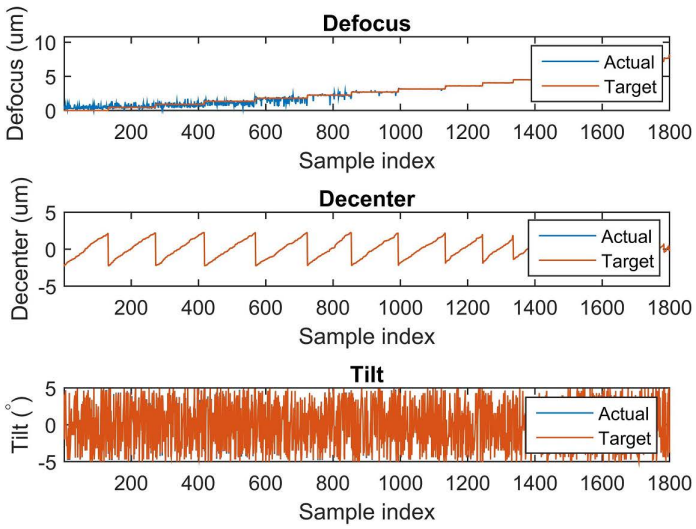

Fig. 5.5 300 µm EFL FAC BP-ANN results obtained with the test set.

1. Manually positioning of the FAC using a micro-gripper with nanometric resolution relying for its alignment only on a visible cameras. This manual pre-alignment can be quite rough since, together with the position in the next step, it necessary only to allow the detector to intercept the beam; however, it usually guarantees an absolute tilt error below 3°.

2. Placing the FAC about 200 µm in front of the diode chip and automatic jogging the FAC towards to the chip until the beam is captured by the beam detector.

3. Acquisition of the beam properties (peak position, centroid position, and so on) from the image captured by the camera and feed them to the trained network; adjustment of the tilt of the FAC according to the predicted tilt from the network and compensation of the movement introduced by the rotation.

4. Repeat the third step but correct the defocus and the decenter instead of the tilt and without further compensations.

All steps except the first one are controlled by the computer. The reason why the control program is not able to adjust the defocus, the decenter and the tilt at the same time is that the FAC could be not exactly at the euleric point of the gripper, so after rotating the gripper, the defocus and the decenter of the FAC could still change even if the movement is compensated.

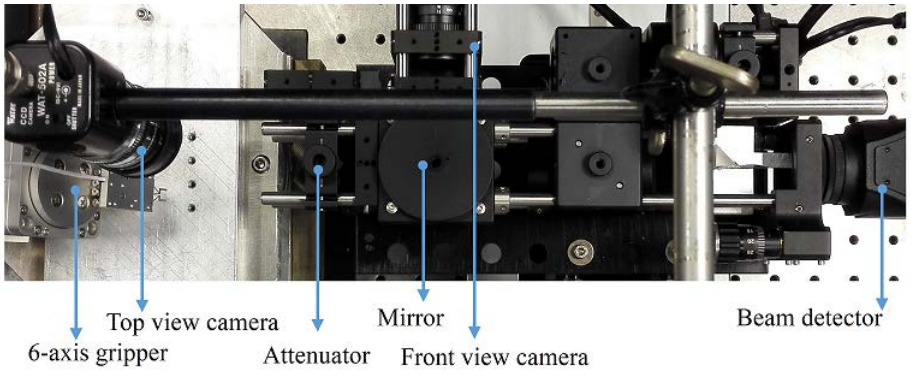

Fig. 5.6 Picture of the experimental setup.

In order to validate the model, five different FACs, namely FAC08-200 (NA:0.8, EFL :200 µm), FAC07-300 (NA:0.7, EFL :300 µm), FAC08-300 (NA:0.8, EFL :300 µm), FAC08-600 (NA:0.8, EFL :600 µm) and FAC05-1100 (NA:0.5, EFL :1100 µm), have been mounted and fully characterized. These five FACs are shown in Fig. 5.7. During the test, the program saved the intensity distribution along the FA, as well as the defocus, the decenter, and the tilt at each step for demonstrating testing results.

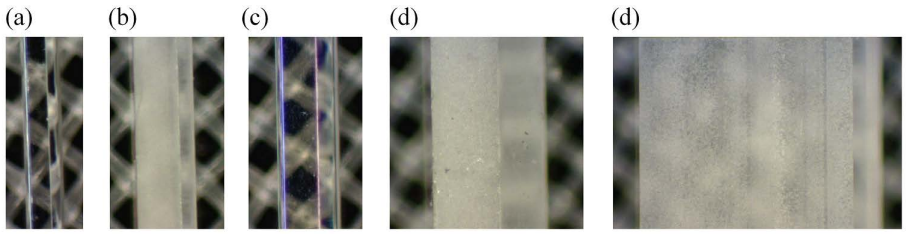

Fig. 5.7 Five different FACs considered for the experimental validation of the assembly procedure: (a) FAC08-200, (b) FAC07-300, (c) FAC08-300, (d) FAC08-600, and (e) FAC05-1100.

5.4.2 Testing results

Fig. 5.8, Fig. 5.9, Fig. 5.10, Fig. 5.11, and Fig. 5.12 report the testing results of FAC08-200, FAC07-300, FAC08-300, FAC08-600, and FAC05-1100, respectively. In each figure the columns represent different two FAC assembly cases, to give an idea of the repeatability. Then, the rows (top to bottom) show the intensity

distribution obtained at the end of the second, third and last steps of the assembling process, respectively.

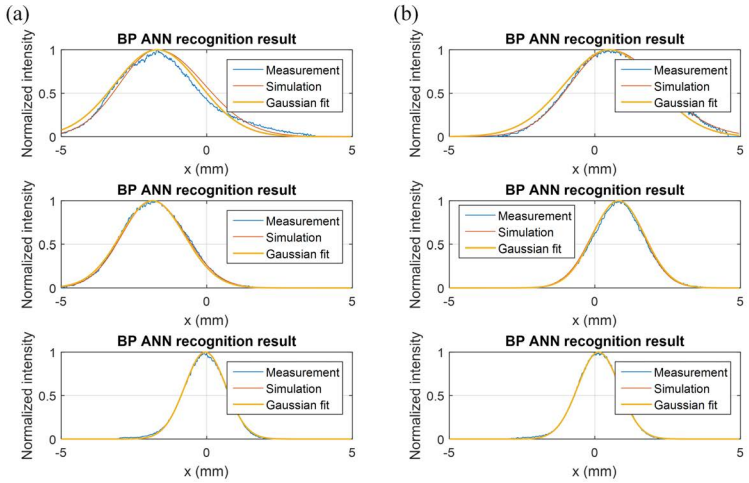

Fig. 5.8 Validation of FAC08-200.

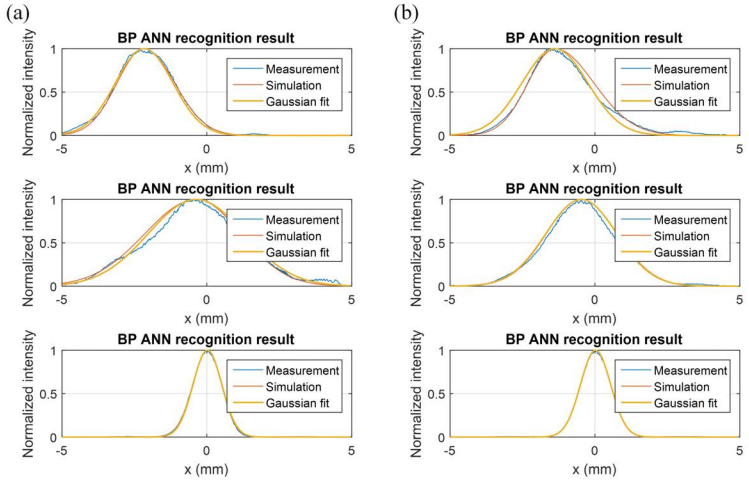

Fig. 5.9 Validation of FAC07-300.

After FAC assembly, the beams are imaged on a NIR camera through a 11 mm EFL aspheric lens. By focusing all beams, it is easy to distinguish the errors. For example, the peak position read from the camera indicates the information of the beam direction and can be used to calculate the decenter error. Fig. 5.13 shows the beam profiles and Tab.5.1 gives the information of the focused beams such as the

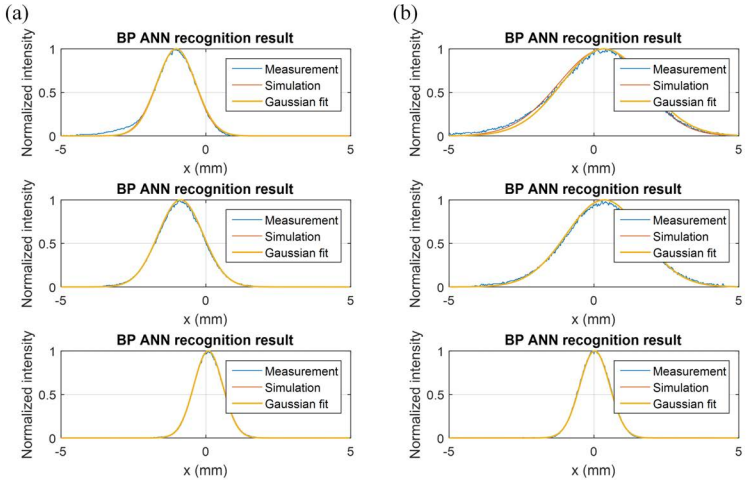

Fig. 5.10 Validation of FAC08-300.

peak position and the waist radius. A linear interpolation is applied to the intensity distributions since the pixel size of the camera is only 4.54 µm, which is too large to indicate the small difference among each beams.

Table 5.1 Peak position and the waist @ $1/e^2$ of each collimated beam in Fig. 5.13.

Case	Peak position (µm)	Waist @ $1/e^2$ (µm)
FAC08-200-(a)	556.78	40.09
FAC08-200-(b)	556.78	41.60
FAC07-300-(a)	558.30	28.74
FAC07-300-(b)	556.78	28.74
FAC08-300-(a)	556.78	26.48
FAC08-300-(b)	561.32	30.26
FAC08-600-(a)	561.32	16.64
FAC08-600-(b)	561.32	16.64
FAC05-1100-(a)	565.86	9.83
FAC05-1100-(b)	561.32	10.59

5.4.3 Discussion of the results

On one hand, Tab. 5.1 indicates that our approach performs well in FAC assembly and it provides accurate enough results in stacking many single emitters and focusing the collimated beams to delivery fiber (usually a around 105 µm of diameter). On

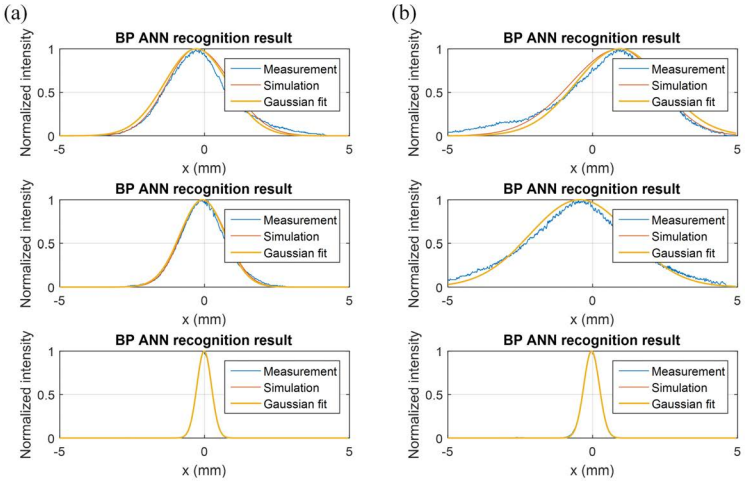

Fig. 5.11 Validation of FAC08-600.

the other hand, Fig. 5.13 highlights some limitations in the model, as detailed in the following.

1. Relatively high bad pointing. The maximal difference of the peak position is 9.08 µm, which indicates the maximal difference of the beam direction is $9.08\,\mu\text{m}/11\,\text{mm} = 0.83\,\text{mrad}$. Excluding the case FAC05-1100-(a), then the accuracy of this approach is compatible to the NF and the FF approach whose best value is 0.1 mrad. There are two factors contributing to the pointing error of our model. The first one is that the BP-ANN only approximately predicts the result. So the model can quickly correct the defocus, the decenter and the tilt without trying to find the optimum position iteratively, but at the cost of a residual misalignment. The second is the NA of the FAC. Small NA means that small misalignment will lead to big beam distortion due to the bad collimation of the marginal part of the beam, high order aberrations and the truncation of the beam, which are not considered in our model. Furthermore, the beam distortion will mislead the trained network. For instance, the second row of the second case in Fig. 5.12 demonstrates how small NA affects the beam shape and the network, which results in inaccurately recognizing and widening by 7% of the spot size compared to the spot size of the first case of FAC05-1100-(a) because of the overcompensation of the defocus. The other example, Fig. 5.14, illustrates the effect of different NA. Obviously, small NA makes the marginal part of the beam not well collimated or cut by the edge of

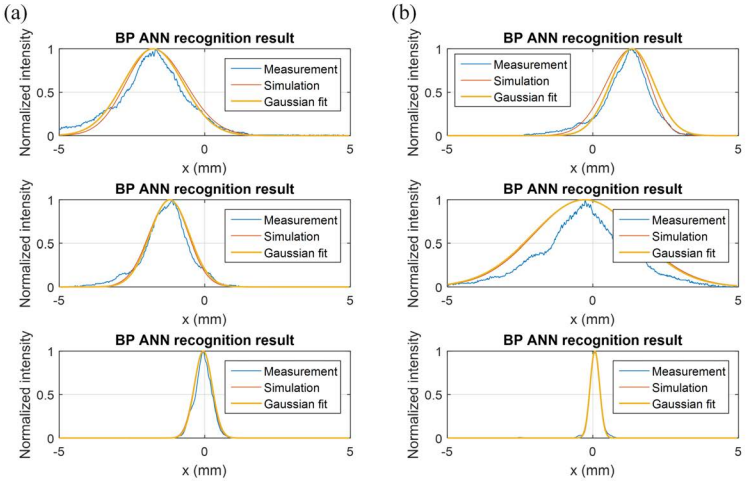

Fig. 5.12 Validation of FAC05-1100.

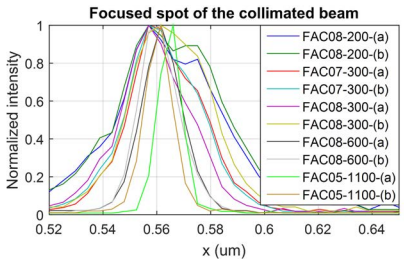

Fig. 5.13 Focused spot intensity distribution of all collimated beams.

FAC, and then the marginal part of the beam generates side lobes. This may increase the focused spot size[54], change the beam shape (demonstrated in Chapter 2) and introduce the power loss if the side lobes are cut during the propagation. In a word, the greater NA (smaller f-number), the better BP-ANN misalignment recognising.

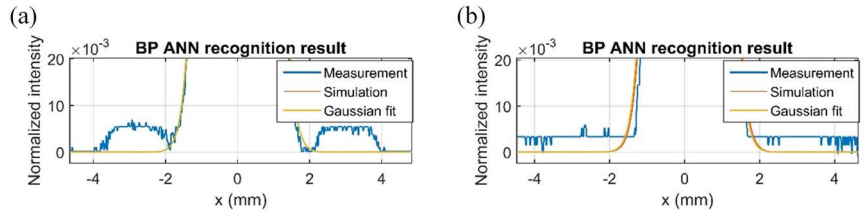

Fig. 5.14 Different NA FACs comparison: (a)FAC07-300 and (b) FAC08-300.

2. Pre-alignment requirement. Fig. 5.15 shows an example in which the beam is distorted by rotating the FAC08-600 by 6° from its optimum position. In this case, the model cannot recognize the beam and it outputs 5°, which is the training upper limit of the tilt. In similar situations the outputs of the network are correct but not accurate.

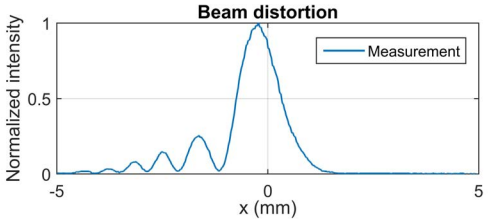

Fig. 5.15 Beam distortion caused by a 6° tilted 600 µm EFL FAC.

3. Over compensations. In the assembly, if FAC is closer to the chip than its best position, two peaks appear. This is the case of the two FAC08-200 cases reported in Fig.5.13. Both FAC08-200-(a) and FAC08-200-(b) have two peaks because smaller EFL FAC is more sensitive to the defocus. But this can be solved by finding the best compensation from the experiment or integrating in the procedure NF measurement capabilities.

4. Inaccurate prediction when assembling large divergence LD chip. The error can be ascribed to the use of the paraxial wave equation (discussed in Ch. 2), from which the Gaussian beam ray-equivalent model is derived.

In summary, using additional measurement setup or employing training data from experiment is necessary for assembling large divergent LD chip with small NA and short EFL FAC so that the BP-ANN is able to provide precise indication.

Chapter 6

Development of a 300 W Module

6.1 Introduction

The design techniques and assembly procedures described in the previous chapters, integrated with extensive thermal and mechanical simulations, have been applied to design and manufacture some prototypes of multi-emitter modules. First devices were based on spatial multiplexing (beam stacking) only and were able to deliver about 100 W; then taking advantage also of polarization and wavelength multiplexing to further scale the power, it has been possible to reach over 300 W in a 105 µm core - 0.22 NA fiber, but with 95% of power in NA = 0.15; moreover, an occupation of just 94 cm^2 leads to a best-in-class footprint figure of 3.2 W/cm^2. These values represent a significant improvement over current state-of-the-art. Given the particularly innovative content, only this module development result is presented in this thesis. This result has been presented at the most important conference for HPLD manufacturers [26].

Considering its small footprint and low ownership costs, this module has been specifically devised as the basic building block of laser sources for metal powder Additive Manufacturing (AM) machines. AM is emerging as the most important fabrication revolution of the last decades because with this approach shape complexity does not imply additional costs and, moreover, the use of material is globally reduced in comparison with traditional technologies[55]. Particular interesting for industrial applications is the laser based manufacturing of metallic parts in which high power laser beams are used to melt metal powders as they are sprayed onto a target

(direct deposition technology) or deposited layer-by-layer on a substrate (powder bed technology)[56]. Today, most of these machines use fiber lasers pumped by a plurality of multi-emitter LD modules for their well known advantages. However, to further widen their adoption, especially to foster the introduction of metal-based AM technologies in micro/small enterprises, a further reduction of sizes and ownership costs of small/mid size machines will be necessary[57]. Laser sources play a key role both for the quality of the AM process and for the determination of its cost; therefore, a dramatic contribution towards the development of smaller and less expensive AM machines comes from the availability of compact LD modules with enough output power and enough brightness to require just few of them per machine.

6.2 Module design and simulation

The target of the design was the development of a multi-emitter laser module demonstrator with about 300 W of output power coupled in a standard 105 µm fiber and with at least 95% of power within NA = 0.15. As a first step the impact of the choices that define the spatial multiplexing stack has been investigated with the model presented in Ch. 4; then, once these are fixed, the overall power has been scaled by polarization and wavelength multiplexing.

Optimizing the spatial stacking of the beams emitted by the single chips composing the multi-emitter module is crucial for the overall beam quality: indeed, besides for the characteristics of the single chips, the beam quality depends on the number of emitters, the distance between two adjacent beams and the optics used to collimate and couple them into the delivery pigtail fiber. Among the different solutions analyzed, taking into account the beam characteristics of the available chips, the most promising were those in the following.

- Spatial combination of 7 emitters with one aspherical fiber coupling lens; this solutions allows having almost 97% of power inside the target 0.15 NA (as shown in the example reported in Fig. 6.1(a)), therefore with best BPP, no power dissipation issues in the output pigtailed ferrule and smallest footprint.
- Spatial combination of 8 emitters with one aspherical fiber coupling lens; this solutions allows increasing both the output power and the brilliance, but implies that at least 3% of the power is dissipated by the pigtail ferrule, with

a possible impact on the package reliability; moreover, the power inside the target 0.15 NA that is reduced to 95%.

- Spatial combination of 9 emitters with two cylindrical fiber coupling lenses with focal lengths optimized for the fast and the slow axis, respectively; this approach allows reaching the highest power and brilliance with limited drawbacks due to ferrule power dissipation, although at the expense of increased assembly process complexity and of bill-of-materials cost.

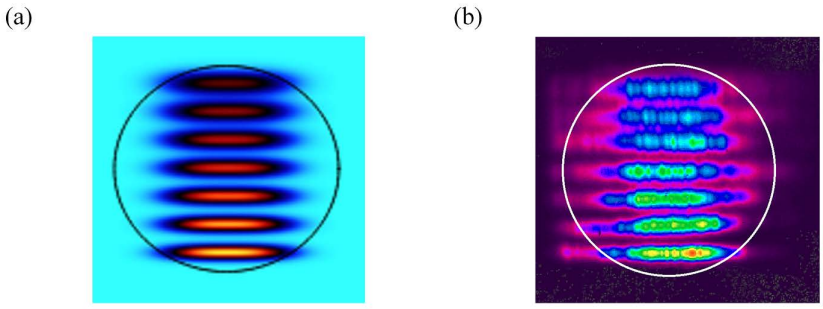

Fig. 6.1 Example of the results obtained by spatial stacking of 7 emitters: comparison of the simulation prediction (left) with the corresponding measurement for one of the first prototypes (right). In both pictures the circle represents the limit for NA = 0.15.

Balancing costs and performance, for the module prototype the configuration that stacks 7 emitters has been chosen. Then, given that the target application of developing a source for "lower cost" direct deposition AM does not pose stringent specifications for the emission spectrum, a "quite coarse" two wavelength scheme for the wavelength multiplexing has been adopted. This choice allowed using unstabilized high power broad area chips and also simplified the dichroic filter design, which now had the only constrain of a reasonably flat spectral response around the two wavelengths to minimize the loss due to wavelength fluctuations. In particular, for the assembly 905 nm and 940 nm emitting chips, with a line width of about 3.5 nm, a wavelength accuracy of ± 10 nm and a wavelength temperature gradient of 0.3 nm/°C have been used. Polarization multiplexing has then been introduced to roughly multiply the power by a factor of 2.

Fig. 6.2 shows the ray tracing analysis of the module architecture prior to geometry optimization to minimize the footprint. The chips in the first and third columns and those in the second and fourth columns have the same wavelength: the beams of the two leftmost columns are combined by the dichroic filter, then their polarization

is rotated by a half wavelength retarder. Similarly for the beams of the two rightmost columns using another dichroic filter, but without polarization rotation. In the end, the two resulting beams are overlapped by a polarization beam splitter and focused into the fiber pigtail. Simulations predicted slightly different power within the NA = 0.15 value for the four beams (namely, 96%, 97%, 95% and 94%), with a combined effect of having within the NA = 0.15 limit the 96% of power.

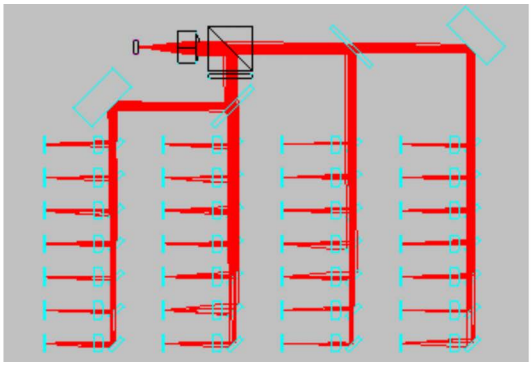

Fig. 6.2 Ray tracing simulation of combination of four columns of seven single emitters exploiting spatial, polarization and wavelength multiplexing.

6.3 Assembly, measurements and analysis

Following the simulation phase, to validate module design some prototypes have been assembled using a custom developed bench that includes a six-axis micro-gripper with nanometric resolution to precisely position the optical components, and visible, IR and thermometric cameras, respectively, to control the placement and to measure NF and FF distributions and thermic maps. The alignments was assisted by the artificial neural network described in Ch. 5. Fig. 6.1(b) reports the measured analogous of the model predictions in Fig. 6.1(a): the excellent agreement provides one of the validation elements for the design tool.

Fig. 6.3(a) shows the power-versus-current characteristics of the demonstrator module. It turned out that the available dichroic filter and polarization beam splitter were not optimized for the wavelengths of the chips, so the operating efficiency is only of about 39% and the maximum power conversion efficiency of about 51%. Besides for the unavoidable excess loss due to the limited polarization extinction ratio typical of wide stripe multi-modes LDs, polarization beam splitter and dichroic

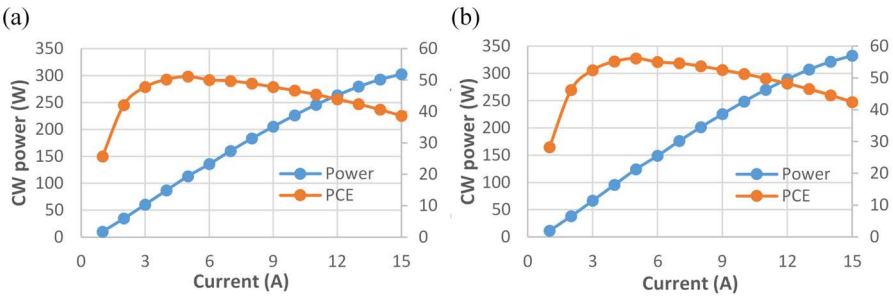

Fig. 6.3 Output power versus input current for a reference module prototype: measurement with "mismatched" polarization beam splitter and dichroic mirror (left), and after compensation of extra losses (right).

filter additional losses caused reaching the target 300 W output power only for 15 A of input current, a working condition that is incompatible with sufficient long-term reliability of the laser chips. However, upon proper optimization of the optical components, the target output power could be reached slightly above 12 A (Fig. 6.3(b)).

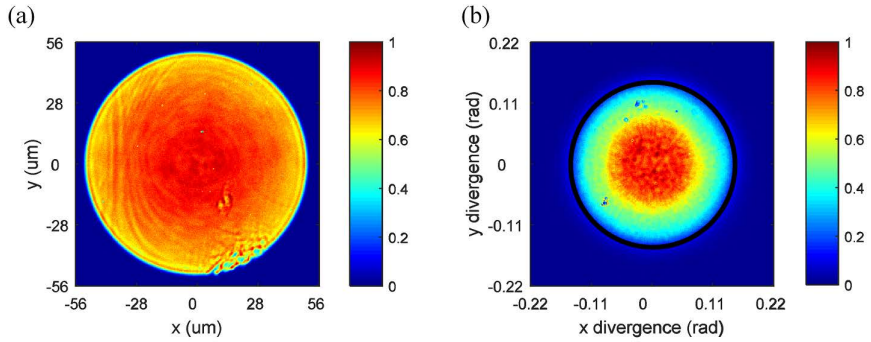

Fig. 6.4 Fiber output characterization at 15 A: NF (left), FF (right).

Fig. 6.4 shows different beam quality characterization pictures taken for 15 A input current: from the NF in Fig. 6.4(a) we evaluated that the actual beam diameter is 104.4 µm, so within the 105 µm fiber core, whereas from the FF in Fig. 6.4(b) that the power in NA = 0.15 (the black circle in the picture) is approximately 95%, in very good agreement with predictions. Fig. 6.5 reports the power fraction against the numerical aperture. The slight discrepancy in the power fraction for NA = 0.15 between simulations and measurements is due to different factors, the most important being that the chip parameters used in the design were measured at 8 A whereas the prototype was characterized at 15 A, and it is well known that the divergence of the slow axis increases with the current. Moreover, LD chips have long tails that were

not considered in our simulation software: for instance, although Fig. 6.1(a) and Fig. 6.1(b) show an excellent match, it is evident that the actual stack has longer tails (Fig. 6.1(b)) than those of the model (Fig. 6.1(a)).

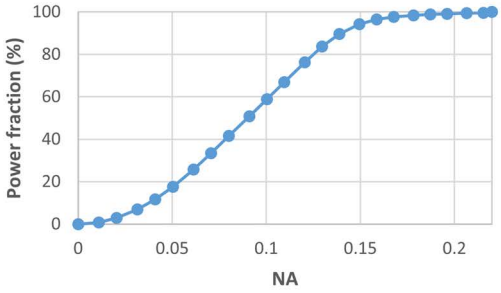

Fig. 6.5 Fiber output characterization at 15 A: power fraction against NA.

Prior to optimization the demonstrator prototype output was 302.8 W at 15 A and 95% of this power was within NA = 0.15, which means that the brightness exceeded 50 $MW/cm^2 - sr$. Thermic maps at 15 A evidenced that the temperature distribution is within safe operating conditions, as also verified from the spectral drift that was within expectations.

Chapter 7

Conclusions and Recommendations

7.1 Conclusions

This thesis was mainly directed at the development of fiber-pigtailed multi-emitter laser-diode modules to be used in material processing laser machines, both as pump for other lasers (mainly fiber lasers) and in direct-diode applications (e.g., welding or cladding).

Multi-emitter modules have experienced a rapid growth in the last years not only in terms of sales, but also of performance, meaning both power level and beam quality. For example, just few years ago the maximum power available from a multi-emitter module was 20 W delivered in a 105 µm/0.22 fiber; today off-the-shelf products are capable of delivering in the same fiber over 150 W. However, a sort of barrier hard to overcome has been reached mainly because, despite such remarkable enhancements, the design of multi-emitter module is still done by "rule-of-thumbs" and using approximations that do not fully take into proper account the impact of all the optical components used in packaging assembly. It is therefore evident that further enhancements can be obtained only by developing new models and this thesis could provide a contribution towards this goal. This is investigated in Ch. 4, which in turn required the preliminary work described in Ch. 2 and in Ch. 3. In particular, Ch. 2 introduces the paraxial Gaussian beam formula and Ch. 3 deals with fundamental issues of the NF and FF characterization of LD chip, and understanding how the paraxial Gaussian beam formula and the aperture truncation affected the precision of measurement. Then, Ch. 4 presents the modeling of laser

beams collimation, propagation and focusing. Optimization example of the model showed that currently used BPP expressions are not accurate enough or can be used only is special cases. Further, it studies how the arrangement of beams affects the maximal number of chips and the power loss.

Furthermore, another important factor to be considered is cost, which is dominated by assembly costs, in terms of materials and time. This thesis aims at providing a contribution also in this field by proposing a new method to speed the assembly the most critical and time consuming optical component. This is tackled in Ch. 5 where the strategy of handling the fast axis collimator is investigated and a new solution that combines Gaussian beam ray tracing and BP-ANN is developed.

7.2 Outcomes

The main achievement has been the design and experimental demonstration of different high-power modules that, by exploiting spatial, wavelength, and polarization multiplexing of a plurality of chips emitting about 10 W each, are able to deliver over 300 W in a 105/0.15 fiber pigtail, figures that represent a remarkable improvement over the current state-of-the-art. The activity has been very challenging because it required the combination of many theoretical, experimental, and technological aspects, not limited to photonics, but including also measurement theory, precision mechanics and thermal management.

The main goal involved also the achievement of other specific results; therefore, the most important outcomes are:

- Development of setups for the NF and FF characterization of LD chips and modules and definition of operation procedures to ensure the consistency of the results.
- Derivation of an accurate formula to evaluate the beam-parameter-product (a parameter defining the quality of emitter beams) of multi-emitter modules, taking into account all the optical components included in the light path.
- Development of a model to predict the performance of multi-emitter LD modules, its validation in actual configurations, and its application to evaluate the

impact of optical, mechanical and thermal tradeoffs for different configurations and architectural choices.

- Investigation of a new method to automatically assemble the fast axis collimator of diode laser chip exploiting a BP-ANN; this approach resulted in a more that halving of the assembly time with respect to currently used automatic machines.

Besides for these main activities, part of the time during the PhD has been also devoted to support the application of high power diode lasers in biomedical applications.

7.3 Recommendations for Future Work

Two main improvements to the principal contributions of the this thesis to the multi-emitter development have already been identified and will constitute the future work, as detailed in the following.

7.3.1 BPP Determination

Although the model for determining the BPP demonstrated very good accuracy even for the limiting cases represented by short EFL FAC (e.g., the 300 µm EFL FAC), the error started to become relevant. This is due to the relatively large beam divergence, in the order of milli-radians, which leads to the enlargement of the beam waist at the entrance of the lens but the model assumes a collimated beam with constant beam waist. In addition, the model does not take the truncation of beams into account, which could cause changes in the focused spot size and coupled power. Therefore, future improvements will have to consider also diverging beams and truncation effects.

7.3.2 Automatic Mounting Strategy

The developed tool based on BP-ANN has been validated with severe and repeated tests and it turned out to be robust and efficient. However, for some cases a slight

deviation from optimal position has been observed. This is mainly due to beam intensity and camera induced noise and will be overcome in future upgrades of the system by adding a beam splitter and integrating the NF monitoring.

References

[1] J Dutta Majumdar and I Manna. Laser material processing. *International materials reviews*, 56(5-6):341–388, 2011.

[2] William E Frazier. Metal additive manufacturing: a review. *Journal of Materials Engineering and Performance*, 23(6):1917–1928, 2014.

[3] Dagmar E Slot, Kirsten H Jorritsma, Charles M Cobb, and Fridus A Weijden. The effect of the thermal diode laser (wavelength 808–980 nm) in non-surgical periodontal therapy: a systematic review and meta-analysis. *Journal of clinical periodontology*, 41(7):681–692, 2014.

[4] Y Liu, R Gassino, A Braglia, A Vallan, and G Perrone. Fibre probe for tumour laser thermotherapy with integrated temperature measuring capabilities. *Electronics Letters*, 52(10):798–800, 2016.

[5] Yu Liu, Hao Yu, Riccardo Gassino, Andrea Braglia, Massimo Olivero, Alberto Vallan, Guido Perrone, and Daniele Tosi. Characterization of tumour laser ablation probes with temperature measuring capabilities. In *BioPhotonics (BioPhotonics), 2015 International Conference on*, pages 1–4. IEEE, 2015.

[6] Yu Liu, Wei Chen, Hao Yu, Riccardo Gassino, Andrea Braglia, Massimo Olivero, Guido Perrone, and A Vallan. All-fiber probe for laser-induced thermotherapy with integrated temperature measurement capabilities. In *SPIE BiOS*, pages 93170W–93170W. International Society for Optics and Photonics, 2015.

[7] Wilhelmus Jacobus Witteman. *The CO2 laser*, volume 53. Springer, 2013.

[8] Allen Nogee. *The Worldwide Market for Lasers: Market Review and Forecast 2015]*. Strategies Unlimited, Mountain View, CA, 2015.

[9] Andreas Siewert. High power industrial grade fiber lasers. https://indico.cern.ch/event/335513/contributions/1724240/attachments/655501/901294/High_Power_Industrial_CW_Fiber_Laser.pdf, (downloaded 03/2017).

[10] Roland Diehl. *High-power diode lasers: fundamentals, technology, applications*, volume 78. Springer Science & Business Media, 2003.

[11] Andrea Braglia, Alessio Califano, Yu Liu, and Guido Perrone. Architectures and components for high power cw fiber lasers. *International Journal of Modern Physics B*, 28(12):1442001, 2014.

[12] Lumentum. 200 w fiber-coupled diode pump laser module. https://www.lumentum.com/sites/default/files/technical-library-items/st2diodepumplaser-ds-cl-ae.pdf, (downloaded 03/2017).

[13] Haiyin Sun. *A practical guide to handling laser diode beams*. Springer, 2015.

[14] Bernd Koehler, Jens Biesenbach, Thomas Brand, Matthias Haag, Sandra Huke, Axel Noeske, Gabriele Seibold, Martin Behringer, and Johann Luft. High-brightness high-power kw system with tapered diode laser bars. In *Lasers and Applications in Science and Engineering*, pages 73–84. International Society for Optics and Photonics, 2005.

[15] Zhihua Huang, Lingling Xiong, Hui Liu, Zhenfu Wang, Pu Zhang, Zhiqiang Nie, Dihai Wu, and Xingsheng Liu. Double-cutting beam shaping technique for high-power diode laser area light source. *Optical Engineering*, 52(10):106108–106108, 2013.

[16] Eva Rodríguez-Vidal, Iban Quintana, Jon Etxarri, Urko Azkorbebeitia, Deitze Otaduy, Francisco González, and Fernando Moreno. Optical design and development of a fiber coupled high-power diode laser system for laser transmission welding of plastics. *Optical Engineering*, 51(12):124301–124301, 2012.

[17] Zuolan Wang, Simon Drovs, Armin Segref, Tobias Koenning, and Rajiv Pandey. Fiber coupled diode laser beam parameter product calculation and rules for optimized design. In *SPIE LASE*, pages 791809–791809. International Society for Optics and Photonics, 2011.

[18] Tso Yee Fan. Laser beam combining for high-power, high-radiance sources. *IEEE Journal of selected topics in Quantum Electronics*, 11(3):567–577, 2005.

[19] Shawn M Redmond, Kevin J Creedon, Jan E Kansky, Steven J Augst, Leo J Missaggia, Michael K Connors, Robin K Huang, Bien Chann, Tso Yee Fan, George W Turner, et al. Active coherent beam combining of diode lasers. *Optics letters*, 36(6):999–1001, 2011.

[20] II-VI Laser Enterprise Laser Diodes Data Sheet. 9w 9xx nm 90um high power single emitter laser diode on c-mount. http://www.laserenterprise.com/resources/pdf/high-power-laser-diodes/ohse/D00466-PB_SEC9-9xx-01_Datasheet_Iss01.pdf, (downloaded 03/2015).

[21] James R Leger. External methods of phase locking and coherent beam addition of diode lasers. *Surface emitting semiconductor lasers and arrays*, pages 379–433, 1993.

[22] Sujatha Ramanujan, Govind P Agrawal, James M Chwalek, and Herbert Winful. Elliptical polarization emission from gaalas laser diodes in an external cavity configuration. *IEEE journal of quantum electronics*, 32(2):213–221, 1996.

[23] Paul Leisher, Kirk Price, Scott Karlsen, David Balsley, Doug Newman, Rob Martinsen, and Steve Patterson. High-performance wavelength-locked diode lasers. In *SPIE LASE: Lasers and Applications in Science and Engineering*, pages 719812–719812. International Society for Optics and Photonics, 2009.

[24] II-VI Laser Enterprise Laser Diodes Data Sheet. 11w 9xx nm 90um high power single emitter laser diode on submount. http://www.laserenterprise.com/resources/pdf/high-power-laser-diodes/ohse/D00470-PB_SES11-9xx-01_Datasheet_Iss01.pdf, (downloaded 02/2017).

[25] Lumentum. Diode lasers, high brightness 10 w, 9xx nm, 63xx series. https://www.lumentum.com/sites/default/files/technical-library-items/63xx_ds_cl_ae.pdf, (downloaded 02/2017).

[26] Hao Yu, Giammarco Rossi, Andrea Braglia, and Guido Perrone. Development of a 300 w 105/0.15 fiber pigtailed diode module for additive manufacturing applications. In *Proc. of SPIE Vol*, volume 10086, pages 100860A–1, 2017.

[27] Hao Yu, Yu Liu, Andrea Braglia, Giammarco Rossi, and Guido Perrone. Investigation of collimating and focusing lenses' impact on laser diode stack beam parameter product. *Applied optics*, 54(34):10240–10248, 2015.

[28] Hao Yu, Giammarco Rossi, Andrea Braglia, and Guido Perrone. Application of gaussian beam ray-equivalent model and back-propagation artificial neural network in laser diode fast axis collimator assembly. *Applied Optics*, 55(23):6530–6537, 2016.

[29] Paul F Goldsmith, Institute of Electrical, Electronics Engineers, Microwave Theory, and Techniques Society. *Quasioptical systems: Gaussian beam quasioptical propagation and applications*. IEEE press New York, 1998.

[30] Shojiro Nemoto. Nonparaxial gaussian beams. *Applied optics*, 29(13):1940–1946, 1990.

[31] Anthony E Siegman. Lasers university science books. *Mill Valley, CA*, pages 664–669, 1986.

[32] Leno S Pedrotti. Basic geometrical optics. pages 99–107, 2012.

[33] Haiyin Sun. Thin lens equation for a real laser beam with weak lens aperture truncation. *Optical Engineering*, 37(11):2906–2913, 1998.

[34] Robert Herloski, Sidney Marshall, and Ronald Antos. Gaussian beam ray-equivalent modeling and optical design. *Applied optics*, 22(8):1168–1174, 1983.

[35] Karl S Kunz and Raymond J Luebbers. *The finite difference time domain method for electromagnetics*. CRC press, 1993.

[36] Wonseok Shin. MaxwellFDFD Webpage, 2015. https://github.com/wsshin/maxwellfdfd.

[37] Julius Adams Stratton. Electromagnetic theory. international series in pure and applied physics, 1941.

[38] Max Born and Emil Wolf. *Principles of Optics, 7-th ed.* 1999.

[39] Joseph W Goodman. *Introduction to Fourier optics, 2nd edition*. McGraw-Hill Publishers, New York, 1996.

[40] LUMENERA INDUSTRIAL CAMERAS. Lw230 & lw235. https://www.lumenera.com/media/wysiwyg/resources/documents/datasheets/industrial/Lw230-Lw235-datasheet.pdf, (downloaded 02/2017).

[41] Haiyin Sun. Measurement of laser diode astigmatism. *Optical Engineering*, 36(4):1082–1087, 1997.

[42] Hao Yu, Giammarco Rossi, Yu Liu, Andrea Braglia, and Guido Perrone. Gaussian beam optics model for multi-emitter laser diode module configuration design. In *Advances in Neural Networks*, pages 457–464. Springer, 2016.

[43] Hao Yu, Giammarco Rossi, Andrea Braglia, and Guido Perrone. Artificial neural network assisted laser chip collimator assembly and impact on multi-emitter module beam parameter product. In *Proc. of SPIE Vol*, volume 10085, pages 1008508–1, 2017.

[44] Flyer and technical specifications FAC. Technical specifications fast axis collimation lenses (fac). http://www.fisba.com/newswriter_files/0000_Produkteflyer_FAC_en_oB.pdf, (downloaded 07/2016).

[45] Fast-axis collimators product data sheet. Fast-axis collimation / fast-axis imaging. http://www.ingeneric.com/wp-content/uploads/2015/12/INGENERIC_FAC.pdf, (downloaded 07/2016).

[46] Thorlabs. https://www.thorlabs.com/newgrouppage9.cfm?objectgroup_id=5840, 2017.

[47] Felix Frischkorn, Joern Miesner, and Sebastian Glass. Full automatic packaging of a hybrid transceiver module. In *Integrated Optoelectronic Devices 2008*, pages 689908–689908. International Society for Optics and Photonics, 2008.

[48] Volker Sturm, Hans-Georg Treusch, and Peter Loosen. Cylindrical microlenses for collimating high-power diode lasers. In *Lasers and Optics in Manufacturing III*, pages 717–726. International Society for Optics and Photonics, 1997.

[49] Jörn Miesner, Andre Timmermann, Jens Meinschien, Bernhard Neumann, Steve Wright, Tolga Tekin, Henning Schröder, Thomas Westphalen, and Felix Frischkorn. Automated assembly of fast-axis collimation (fac) lenses for diode laser bar modules. In *SPIE LASE: Lasers and Applications in Science and Engineering*, pages 71980G–71980G. International Society for Optics and Photonics, 2009.

[50] J Pierer, M Lützelschwab, S Grossmann, G Spinola Durante, Ch Bosshard, B Valk, R Brunner, R Bättig, and N Lichtenstein. Automated assembly processes of high power single emitter diode lasers for 100w in 105 μm/na 0.15 fiber module. In *SPIE LASE*, pages 79180I–79180I. International Society for Optics and Photonics, 2011.

[51] C Brecher, N Pyschny, S Haag, and V Guerrero Lule. Automated alignment of optical components for high-power diode lasers. In *Proc. SPIE*, volume 8241, page 82410D, 2012.

[52] Thomas Westphalen, Stefan Hengesbach, Carlo Holly, Martin Traub, and Dieter Hoffmann. Automated alignment of fast-axis collimator lenses for high-power diode laser bars. In *SPIE LASE*, pages 89650V–89650V. International Society for Optics and Photonics, 2014.

[53] David E Rumelhart, Geoffrey E Hinton, and Ronald J Williams. Learning representations by back-propagating errors. *Nature*, 323:533–536, 1986.

[54] Hakan Urey. Spot size, depth-of-focus, and diffraction ring intensity formulas for truncated gaussian beams. *Applied optics*, 43(3):620–625, 2004.

[55] Samuel H Huang, Peng Liu, Abhiram Mokasdar, and Liang Hou. Additive manufacturing and its societal impact: a literature review. *The International Journal of Advanced Manufacturing Technology*, pages 1–13, 2013.

[56] Lawrence E Murr, Sara M Gaytan, Diana A Ramirez, Edwin Martinez, Jennifer Hernandez, Krista N Amato, Patrick W Shindo, Francisco R Medina, and Ryan B Wicker. Metal fabrication by additive manufacturing using laser and electron beam melting technologies. *Journal of Materials Science & Technology*, 28(1):1–14, 2012.

[57] Peter Dorrington, Franck Lacan, and Samuel Bigot. How are micro enterprises adopting emergent technologies? In *Sustainable Design and Manufacturing 2016*, pages 215–226. Springer, 2016.

Appendix A

Proof of Beam Profile on Focal Plane

Considering for instance 2 incident beams of amplitude $A(x)$, the expression of the combination of the 2 beams entering the lens is

$$A_{\text{all}}(x) = A(x)\exp(j\phi_1) + A(x + x_{\text{offset}})\exp(j\phi_2) \tag{A.1}$$

being x_{offset} the distance between the two diodes, $A(x)$ the amplitude of a single beam at the front focal plane, and ϕ_1 and ϕ_2 the phases of two beams, respectively.

The amplitude at the back focal plane is the Fourier Transform of Eq. A.1, which is

$$A'_{\text{all}}(f_{\text{x}}) = A'(f_{\text{x}})\left[\exp(j\phi_1) + \exp(-2\pi j x_{\text{offset}} f_{\text{x}})\exp(j\phi_2)\right] \tag{A.2}$$

where $A'(x)$ is the Fourier Transform of a single beam at the focal plane.

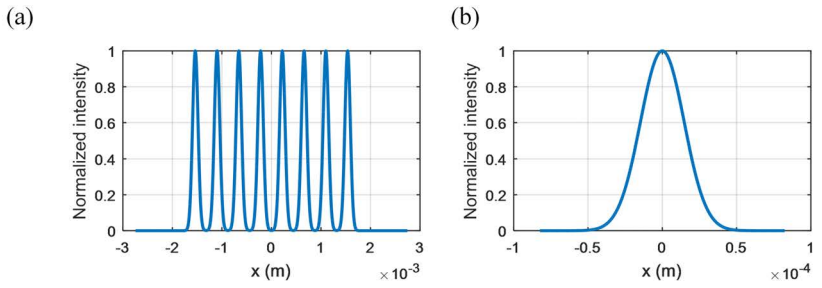

Fig. A.1 Intensity distribution of 8 incoherent beams: (a) at the entrance of the lens, and (b) on the focal plane of the lens.

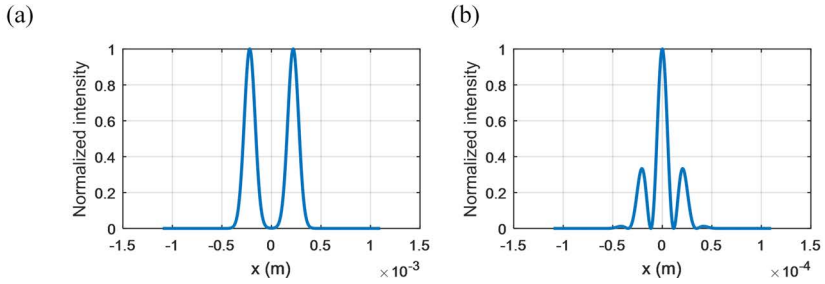

Fig. A.2 Intensity distribution of 2 coherent beams: (a) at the entrance, and (b) on the focal plane.

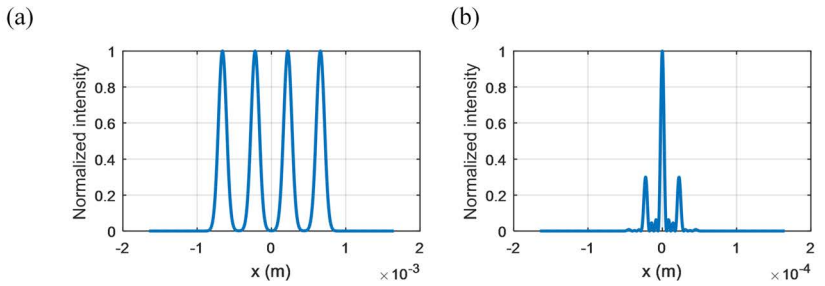

Fig. A.3 Intensity distribution of 4 coherent beams: (a) at the entrance, and (b) on the focal plane.

The intensity at the focal plane becomes

$$|A'_{\text{all}}(f_{\text{x}})|^2 = |A'(f_{\text{x}})|^2[2+\exp(-2\pi j x_{\text{offset}} f_{\text{x}} - j\triangle\phi)+ \exp(2\pi j x_{\text{offset}} f_{\text{x}} + j\triangle\phi)] \tag{A.3}$$

where f_{x} is the spatial frequency, and $\triangle\phi$ is the phase difference between ϕ_1 and ϕ_2.

Since the two beams are incoherent, the phase difference $\triangle\phi$ is random and Eq. A.3 reduces $|A'_{\text{all}}(f_{\text{x}})|^2 = 2|A'(f_{\text{x}})|^2$. Extending the result to N beams, the resulting intensity is

$$|A'_{\text{all}}(f_{\text{x}})|^2 = |A'(f_{\text{x}})|^2 \left\{ N + \sum_{\text{m}=0}^{\text{N}-1} \exp[-2m\pi j x_{\text{offset}} f_{\text{x}}] \cdot \sum_{\text{n}=0,\text{n}!=\text{m}}^{\text{N}-1} \exp[2n\pi j x_{\text{offset}} f_{\text{x}}] \exp[j(\phi_{\text{n}} - \phi_{\text{m}})] \right\} \tag{A.4}$$

Hence, for N incoherent beams the intensity on the focal plane is $N|A'(f_{\text{x}})|^2$ and thus the spot size of N beams is identical to the spot of a single beam, the difference

being only in the intensity. Fig. A.1 refers to the distribution of $N = 8$ incoherent beam.

It is easy to learn from the proof above that if all beams are coherent, the number of laser diodes that can be coupled in to the fiber is unlimited. Some examples of coherent beams focusing are demonstrated in Fig. A.2, A.3 and A.4.

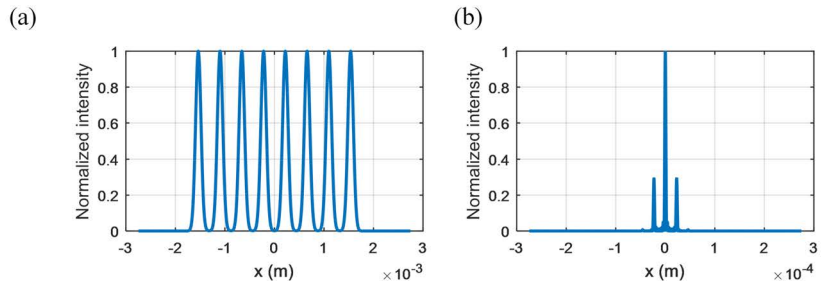

Fig. A.4 Intensity distribution of 8 coherent beams: (a) at the entrance, and (b) on the focal plane.

Appendix B

Acronyms

AM Additive Manufacturing. 71–73

AR Anti-Reflection. xiii, 52

BFL Back Focal Length. 25, 56

BP-ANN Back-Propagation Artifical Neural Network. viii, xiii, 14, 58–62, 64, 68–70, 78, 79

BPP Beam Parameter Product. ix, 5–9, 13–15, 17, 24, 38, 40–42, 46–49, 51, 72, 78, 79

CBC Coherent Beam Combining. 8

CCD Charge-Coupled Device. xi, 24–27, 29, 34, 44

CoC Chip on Carrier. 4

CW Continuous Wave. 1, 8

EFL Effective Focal Length. xii–xv, 17–19, 26, 27, 32, 34–36, 39–41, 44–49, 51, 53, 54, 56–58, 62–66, 70, 79

FA Fast Axis. xi–xiii, 6, 7, 9, 15, 26, 27, 29, 30, 33–41, 45, 47–49, 52, 53, 56, 57

FAC Fast Axis Collimator. viii, xii–xv, 9, 10, 35, 38–41, 43–49, 52, 56–60, 62–70, 79

FBG Fiber Bragg Grating. 3

FDFD Finite-Difference Frequency-Domain. 21

FF Far Field. vii, xi, xii, xiv, 7, 14, 17, 19, 21–25, 27–30, 33–35, 39, 58, 63, 68, 74, 75, 77, 78

FFL Front Focal Length. 25

FL Fiber Laser. 1, 2, 4

HPLD High Power semiconductor Laser Diode. 3–5, 25, 37, 71

HR High-Reflectance. xiii, 52

LD Laser Diode. x, xii, xiii, 6, 7, 9, 11–15, 17, 25, 37, 38, 43, 44, 57, 70, 72, 75, 77, 78

LDs Laser Diodes. xii, 3, 15, 38, 39, 41, 44, 56, 74

NA Numerical Aperture. xiii, xiv, 33, 34, 39, 46–48, 50, 51, 56, 68–76

ND Neutral Density. 25

NF Near Field. vii, xi, xii, xiv, xv, 14, 17, 21, 22, 24–27, 30–32, 34, 35, 37, 39, 58, 63, 68, 70, 74, 75, 77, 78, 80

NIR Near Infrared. 24, 63, 66

OE Optical Engine. 3, 4

SA Slow Axis. xi, xii, 6, 7, 9, 15, 26, 27, 29, 30, 37–39, 41, 45, 47–49, 52

SAC Slow Axis Collimator. xii, xiii, 9, 10, 38, 41, 43, 46, 48, 51, 52

TE Transverse Electric. 10, 11